Journal of Petrology, 2026, **67**(11), egag099
https://doi.org/10.1093/petrology/egag099
Published: 14 NOVEMBER 2026
Original Manuscript

OXFORD

Quantitative Petrography from Thin-section Videos: A Unified Optical Workflow for Grain-scale Microstructure Analysis

TAN FURUKAWA* and TATSUKI TSUJIMORI

Department of Earth Science, Graduate School of Science, Tohoku University, 6-3 Aramaki-Aza-Aoba, Aoba-Ku, Sendai 980-8578, Japan

*Corresponding author. Telephone: +81-22-795-6615. E-mail: tan.furukawa.b4@tohoku.ac.jp
†Handling Editor: Prof. Pierre Lanari

Quantitative microstructural analysis of petrographic thin sections often requires separate instruments and workflows for grain segmentation, mineral identification, and crystallographic orientation. Here, we present a largely automated workflow that derives these measurements using only a conventional rotating-stage polarizing microscope and camera. The workflow begins with the acquisition of a continuous 360° video of a thin section under crossed polars during manual rotation of the microscope stage. The video is automatically converted into a maximum-intensity image and an extinction-angle map, from which grains are segmented based on differences in optically inferred *c*-axis orientation, and grain size, shape, and grain-shape orientation are quantified. The resulting grain segmentation also enables semi-supervised mineral classification from a limited number of user-labeled grains. For low-retardation uniaxial minerals, additional λ-plate measurements and a small stage tilt resolve optical ambiguities and provide three-dimensional *c*-axis orientations. Comparison with electron backscatter diffraction (EBSD) shows that the optical workflow reproduces grain boundaries, grain-scale statistics, and *c*-axis fabrics most reliably for thin sections ∼20–35 μm thick and with a 5° segmentation threshold. Its main limitations arise from boundary mixing in thicker thin sections and weak optical contrast between neighboring grains. The workflow is implemented in NicoNavi, which integrates mineral classification, grain morphology, and crystallographic orientation within a common grain-scale dataset. This approach provides a practical framework for reproducible quantitative petrography using conventional thin sections without specialized microanalytical instrumentation such as EBSD.

Keywords crystal preferred orientation, grain segmentation, microstructure, optical petrography, quartz

Introduction

Rock microstructures provide quantitative information on tectonic and metamorphic processes through grain-scale descriptors such as grain shape, spatial arrangement, chemical composition, and crystallographic orientation. These descriptors form the basis for kinematic analyses and quantitative characterization of metamorphic and deformation-related fabrics (e.g. Xypolias, 2010; Ortolano *et al.*, 2020; Roda *et al.*, 2021; Caso *et al.*, 2024). Such quantitative microstructural analyses are supported by a wide range of analytical techniques. For example, chemical and mineralogical distributions can be characterized using electron-beam X-ray mapping (de Andrade *et al.*, 2006; Friel & Lyman, 2006; Lanari *et al.*, 2019). Crystallographic orientations can be determined using electron backscatter diffraction (EBSD; Prior *et al.*, 1999). Although these techniques provide detailed microstructural information, mapping large areas can be time-consuming (Lanari *et al.*, 2019; Winiarski *et al.*, 2021). By contrast, polarized-light microscopy is relatively inexpensive, widely available, and routinely used to examine conventional petrographic thin sections. It provides information on grain boundaries, mineral phases, grain morphology, and crystallographic orientation.

The potential of polarized-light microscopy for quantitative analysis has long been recognized, and several digital approaches emerged in the early 1990s. A major advance was computer-integrated polarization microscopy (CIP), which used images acquired at different polarization angles to map quartz *c*-axis orientations and delineate grain boundaries based on local orientation differences (Heilbronner & Pauli, 1993); simplified implementations were subsequently developed (Stöckhert & Duyster, 1999). During the same period, optical images began to be used for automated and semi-automated grain segmentation (Heilbronner, 2000; Zhou *et al.*, 2004; Roy Choudhury *et al.*, 2006) and mineral classification (Launeau *et al.*, 1994). Image acquisition also became increasingly automated. Computer-controlled rotating polarizers enabled systematic imaging at multiple polarization angles and were applied to grain-boundary detection (Goodchild & Fueten, 1998) and quartz *c*-axis analysis (Fueten & Goodchild, 2001).

Recent advances in image processing and machine learning have further increased the potential of optical microscopy for quantitative petrography, particularly because of its accessibility and efficiency. Examples include automated grain segmentation in sedimentary rocks (Jiang *et al.*, 2018; Chen *et al.*, 2024; Zheng *et al.*, 2024) and

RECEIVED DECEMBER 16, 2025. **REVISED** OCTOBER 30, 2026. **ACCEPTED** NOVEMBER 3, 2026
© The Author(s) 2026. Published by Oxford University Press.
This is an Open Access article distributed under the terms of the Creative Commons Attribution License (https://creativecommons.org/licenses/by/4.0/), which permits unrestricted reuse, distribution, and reproduction in any medium, provided the original work is properly cited.

Downloaded from academic.oup.com/petrology/article/67/11/egag099/9022254 by Hogaku-Bu Library user on 25 November 2026

mineral recognition from polarized reflected-light images (Iglesias *et al.*, 2011).

Building on these developments, quantitative petrographic workflows have progressively integrated grain geometry with mineralogical and crystallographic information. Early geographic information system (GIS)-based approaches linked segmented grains with spatially referenced morphometric and compositional data (Barraud, 2006; Li *et al.*, 2008), while the Microscopic Information System (MIS) combined thin-section imaging, grain segmentation, morphometric measurements, and modal analysis (Tarquini & Favalli, 2010). More recent workflows have incorporated additional mineralogical and crystallographic information. For example, the ArcGIS-based MicroFabric Analyzer (MFA) toolbox integrates optical grain geometry with X-ray-map-based mineral identification (Visalli *et al.*, 2021), while the pipeline for optic-axis mapping (POAM) software combines multi-angle polarized-light imaging with grain segmentation, mineral classification, and optic-axis mapping (Acevedo Zamora *et al.*, 2024). Commercial systems such as ZEISS Axioscan 7 Geo/PetPAT provide further automation of whole-slide imaging, mineral classification, and grain and orientation analysis (Carl Zeiss Microscopy GmbH, 2024).

Despite these advances, existing workflows differ substantially in the types of information they provide, their hardware requirements, and their degree of automation (Table 1). In particular, no single workflow currently integrates full *c*-axis orientation determination with grain segmentation, mineral identification, and morphometric analysis within a unified analytical environment. Consequently, quantitative petrographic analysis often requires multiple independent tools and processing steps, complicating data integration and efficient application to large datasets. To address this limitation, we developed a unified software environment, NicoNavi, that integrates these analytical steps into a single end-to-end workflow, enabling reproducible and efficient quantitative analysis of petrographic thin-section images.

Overview of the video-based optical workflow

The extinction behavior and birefringence of a mineral encode its crystallographic orientation and optical properties. These signals can be recovered by monitoring changes in interference color while the thin section is rotated on the microscope stage (Heilbronner & Pauli, 1993; Stöckhert & Duyster, 1999; Fueten & Goodchild, 2001). Here, we capture these changes continuously as a video. The workflow proposed in this study (Fig. 1) uses short videos acquired during continuous 360° stage rotation and, for the tilt measurements, during focus sweeps to analyze these color changes. This video-based approach minimizes hardware requirements and streamlines data acquisition. For example, it replaces the stepwise acquisition of discrete multi-angle images used in previous optical workflows, including manual acquisition at fixed stage increments (Heilbronner & Pauli, 1993; Acevedo Zamora *et al.*, 2024) and acquisition with computer-controlled rotating polarizers (Goodchild & Fueten, 1998; Fueten & Goodchild, 2001).

The workflow consists of three connected subprocesses: grain segmentation, estimation of *c*-axis orientation, and classification of segmented grains. These subprocesses are integrated into the software NicoNavi, and their flowcharts are shown in Fig. 1.

For grain segmentation, we propose a grain-segmentation method based on thresholding optically inferred orientation differences, analogous to misorientation-based grain segmentation in EBSD (e.g. Bachmann *et al.*, 2011; Muto *et al.*, 2011; Heilbronner & Kilian, 2017). Because impurities, imaging noise, and finite-thickness boundary effects can cause segmentation or orientation errors in natural thin sections, we also developed image- and boundary-cleaning algorithms for thin-section images. Their performance and limitations are evaluated against EBSD data in the section *Accuracy and limitations of optical grain segmentation*.

To estimate *c*-axis orientations, we extend previous methods for estimating azimuth and inclination (Heilbronner & Pauli, 1993; Stöckhert & Duyster, 1999; Fueten & Goodchild, 2001). The extinction angle, β_{ex}, and retardation at each pixel constrain the *c*-axis azimuth, φ, and inclination, θ, respectively. Cross-polarized light (XPL) observations alone, however, do not provide a unique orientation: both φ and $\varphi + 90°$ produce extinction during stage rotation, while θ and $180° - \theta$ produce the same retardation. Previous studies have resolved these ambiguities using a λ-plate for azimuth (Heilbronner & Pauli, 1993; Stöckhert & Duyster, 1999; Acevedo Zamora *et al.*, 2024) and stage tilting for inclination (Heilbronner & Pauli, 1993; Heilbronner & Barrett, 2014). We adopt similar optical principles to predict XPL + λ-plate interference colors from the optical configuration. Unlike CIP, which uses quartz thin sections of ~20–25 μm to obtain first-order-white interference colors (Heilbronner & Barrett, 2014), our calibration allows the method to be applied to conventionally prepared thin sections of ~30 μm. We also provide a 3D-printable tilting stage to standardize the tilting procedure (Furukawa, 2026*a*).

For grain classification, we use the segmented grains obtained from the grain-segmentation step as units for semi-supervised mineral classification. Each grain is represented by shape, size, and color features, and the user assigns mineral labels to a limited number of representative grains. These labels are extended to the remaining grains according to feature-space similarity. The resulting mineral labels can then be combined with the grain morphology from the segmentation step and the orientation information from the *c*-axis orientation estimation step, allowing grain-specific analyses of grain size, grain-shape orientation, and crystallographic orientation within the same workflow.

Samples and data acquisition

All rotation videos were recorded using an Olympus BX53 polarizing microscope under XPL, with video acquisition controlled using cellSens Standard v4.2.1. The samples comprised orthoquartzite from Gengelegengele Gorge, Tanzania (GGG2, thickness 45 μm; GGG3, 22 μm; GGG4, 35 μm; GGG5, 33 μm; GGG6, 43 μm), piemontite schist from the Yamagami metamorphic rocks, Japan (YM3, 35 μm), and a synthetic quartz thin section (W1415, 25 μm; Muto *et al.*, 2011). Thin-section thickness was measured 10 times with a dial test indicator (Mitutoyo, TI-112HLX, Code No. 513-435-10H; graduation: 2 μm), and the mean value was used. EBSD maps of the same areas were acquired using a JEOL JSM-7001F field-emission scanning electron microscope with an Oxford Instruments NordlysNano detector. The GGG thin sections were mapped at 15 kV, 70° specimen tilt, a nominal magnification of 160×, a working distance of 25 mm, and a step size of 2 μm, indexing against quartz and calcite; the indexing rate was 89–97%. All EBSD orientation data were converted to inclination and azimuth using MTEX 5.11.2 (Bachmann *et al.*, 2010).

For each field of view, five videos were recorded (Fig. 1). The first two were continuous 360° rotation videos acquired by hand over ~1 min: one under XPL alone and one under XPL with the λ-plate

Downloaded from academic.oup.com/petrology/article/67/11/egag099/9022254 by Hogaku-Bu Library user on 25 November 2026

Table 1 Comparison of petrographic image-analysis methods.

Method	Dedicated hardware required	Mineral/phase identification	Grain segmentation	Grain size and shape analysis	Orientation analysis	Automation/whole thin-section analysis
ZEISS Axioscan 7 Geo + PetPAT[1]	Yes, Axioscan 7 Geo slide scanner	Yes, user-trained ML classification	Yes, extinction-angle based	Yes, via ZEN Image Analysis/PetPAT	Partial, extinction-angle based; *c*-axis azimuth ambiguous by 90°; inclination not determined	Automated whole-slide acquisition and batch analysis
CIP[2]	No, standard rotating-stage polarizing microscope; optional optical components	No, target phase must be known; mainly uniaxial minerals	Yes, *c*-axis orientation-difference based	Yes, via integrated Image SXM tools	Yes, full *c*-axis orientation	Computerized image analysis; multi-angle and tilt images acquired manually
AAVA (AvaGenerator/ StereoNett)[3]	No, standard rotating-stage polarizing microscope	No, quartz only	Partial, *c*-axis orientation-difference-based boundary extraction	No, requires separate image analysis	Partial, *c*-axis azimuth and inclination; 180° azimuth ambiguity; dip direction unresolved	Automated image processing; microscope stage rotated manually; field-of-view based
MIS[4]	Yes, slide scanner with custom polarization mount	Yes, manually assigned by user	Yes, region-growing based; manual refinement	Yes, area, perimeter, and size distribution	No	Whole thin-section scanning and automated segmentation; manual refinement and mineral assignment required
MFA[5]	Yes, optical scanner; μXRF for phase identification	Yes, μXRF/Q-XRMA-based mineral classification	Yes, color-based; manual refinement	Yes, multiple size and shape descriptors	No, grain-shape orientation only	Semi-automated whole thin-section processing; manual parameter tuning
Fueten rotating polarizer stage/GeoVision[6]	Yes, computer-controlled rotating polarizer stage	Yes, ANN-based classification	Yes, gradient-based; manual correction may be required	Yes, grain size, area, and shape measurements from closed grain-boundary maps	Partial, *c*-axis azimuth and inclination; 180° azimuth ambiguity; dip direction unresolved	Automated polarizer rotation, image acquisition
POAM[7]	No, standard rotating-stage polarizing microscope and camera; λ-plate required	Yes, supervised object-based classification	Yes, object-based region merging; manual parameter tuning	Yes, grain size and shape descriptors	Partial, *c*-axis azimuth and inclination; dip direction unresolved	Semi-automated image processing; microscope stage rotated manually; field-of-view based
NicoNavi (this study)	No, standard rotating-stage polarizing microscope and camera; λ-plate and optional tilt stage for full *c*-axis orientation	Yes, semi-supervised grain classification from user-labeled examples	Yes, optical-orientation-difference based	Yes, grain size, shape, and grain-shape orientation	Yes, full *c*-axis orientation	Automated video processing; microscope stage rotated manually; field-of-view based

For 'Orientation analysis', Yes indicates that the full three-dimensional *c*-axis orientation can be uniquely resolved; Partial indicates that *c*-axis information is obtained but remains incomplete or ambiguous. ML = machine learning; ANN = artificial neural network; μXRF = micro-X-ray fluorescence.

[1] Carl Zeiss Microscopy GmbH (2024).
[2] Heilbronner & Pauli (1993), Heilbronner (2000), Heilbronner & Barrett (2014).
[3] Stöckhert & Duyster (1999).
[4] Tarquini & Favalli (2010).
[5] Ortolano *et al.* (2018), Visalli *et al.* (2021).
[6] Fueten (1997), Goodchild & Fueten (1998), Fueten & Goodchild (2001), Thompson *et al.* (2001).
[7] Acevedo Zamora *et al.* (2024).

Downloaded from academic.oup.com/petrology/article/67/11/egag099/9022254 by Hogaku-Bu Library user on 25 November 2026

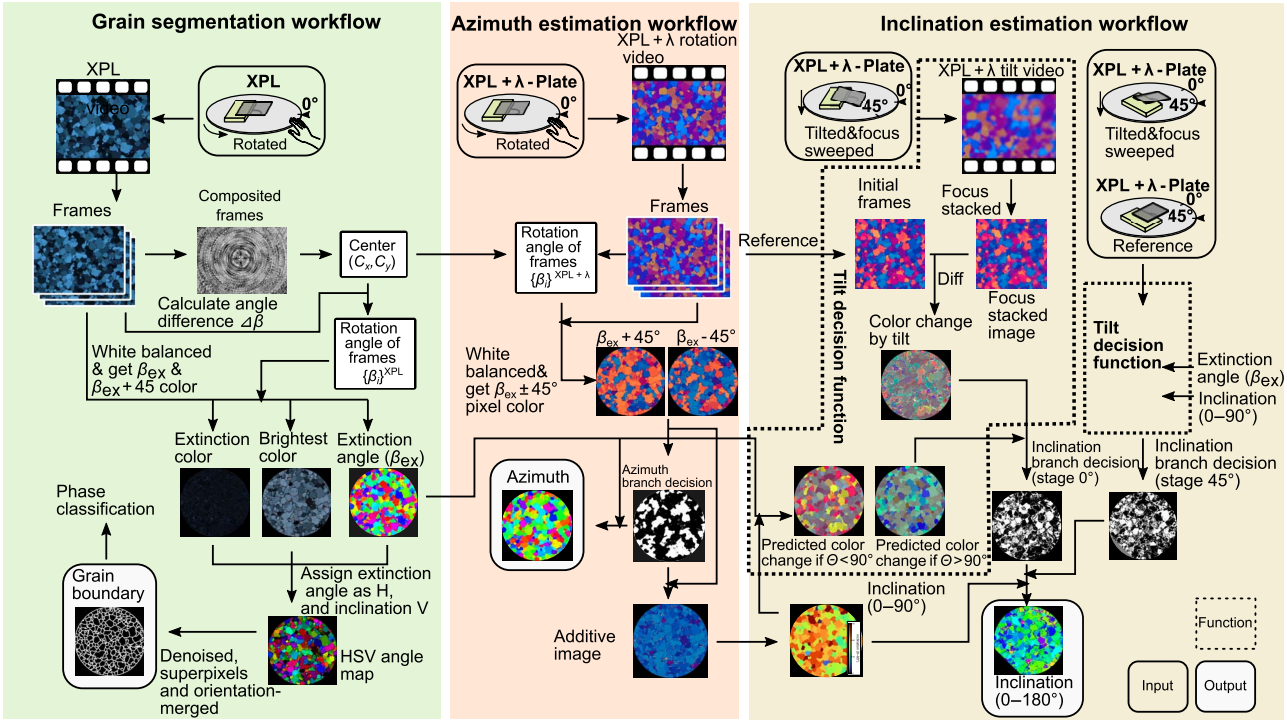


Figure 1 Overview of the proposed thin-section analysis workflow.

inserted. The next two videos recorded the response to a 7° stage tilt introduced using the 3D-printable tilting stage shown in Fig. 10, which was fixed to the microscope stage with double-sided tape. With the λ-plate inserted, an ∼10 s focus-sweep video was recorded at each of two stage positions, 0° and 45°. Finally, a 1 s reference video was recorded at 45° after returning the tilting stage to horizontal, providing pre-tilt colors for comparison with tilted images. All videos were recorded at 20 fps.

The red, green, and blue (RGB) intensity values were corrected within NicoNavi using a gray-world correction, a white-balancing method that assumes equal mean intensities across the red, green, and blue channels (Buchsbaum, 1980). Red, green, and blue channels were rescaled so that their field-of-view mean values were equal, with scaling factors estimated from the first frame of the XPL rotation video. Because interference colors also contribute to the field mean, a full correction would remove part of the measured color signal; the correction was therefore applied at half strength. The same factors were applied to all videos from a given field of view.

Grain segmentation

Stage rotation-center estimation

For each field of view, a short video recorded during continuous 360° stage rotation was subsampled into 100 frames for analysis (Fig. 2a). Because the stage-rotation axis does not necessarily coincide with the image center, we first determined its position in image coordinates.

Each frame was converted to grayscale, and a composite image was generated by selecting the maximum value across the 100 frames at each pixel (Fig. 2b). This image was enhanced by global histogram equalization. The stage-rotation center was then detected using the fast radial symmetry transform (Ni *et al.*, 2012) to define an initial estimate $c_0 = (x_0, y_0)$, which was refined by four-fold symmetry scoring to obtain $c_1 = (x_1, y_1)$ (Supplementary Sections S1.1 and S1.2).

Because only the largest circle centered at c_1 remains within the image throughout the full 360° rotation (Fig. 2a and b), subsequent analyses were restricted to this circular region.

Extinction-angle map and maximum-intensity image

At each pixel, the grayscale intensity under XPL varies approximately sinusoidally with the stage angle $\beta \in [0°, 360°)$, reaching minima at extinction and maxima ∼45° from extinction (Fig. 3).

Because extinction occurs four times during a 360° rotation, we identified the intensity minimum separately within $[0°, 90°)$, $[90°, 180°)$, $[180°, 270°)$, and $[270°, 360°)$. The four estimates were reduced modulo 90° to obtain β_{ex}^1, β_{ex}^2, β_{ex}^3, and β_{ex}^4. The extinction angle was then defined as

$$\beta_{ex} = \arg\min_{\beta} \left\{ \left|\beta - \beta_{ex}^1\right| + \left|\beta - \beta_{ex}^2\right| + \left|\beta - \beta_{ex}^3\right| + \left|\beta - \beta_{ex}^4\right| \right\}, \quad (1)$$

where $|\cdot|$ denotes angular difference modulo 90°. This minimization combines the four extinction estimates into a single robust extinction angle for each pixel. The color at β_{ex} defines the extinction-color map (D; Fig. 4b), whereas the color at β_{ex} + 45° defines the maximum-intensity image (M; Fig. 4c). The corresponding β_{ex} values form the extinction-angle map (B; Fig. 4d). The extinction-angle map and maximum-intensity image are subsequently used for grain segmentation.

Optical orientation mapping in HSV space

Our grain-segmentation method separates grains based on differences in *c*-axis orientation. The maximum-intensity image (M; Fig. 4c) and extinction-angle map (B; Fig. 4d) provide complementary information

Downloaded from academic.oup.com/petrology/article/67/11/egag099/9022254 by Hogaku-Bu Library user on 25 November 2026

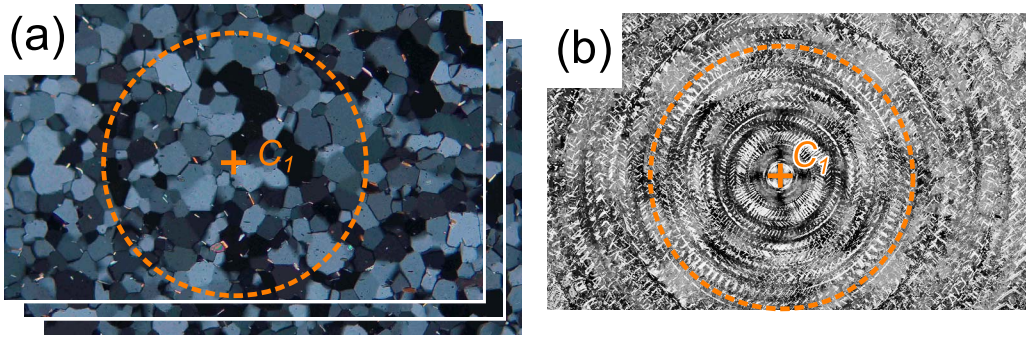


Figure 2 (a) Representative frames acquired during stage rotation and (b) the composite image used to estimate the rotation center. The dashed circle indicates the region retained for subsequent analysis.

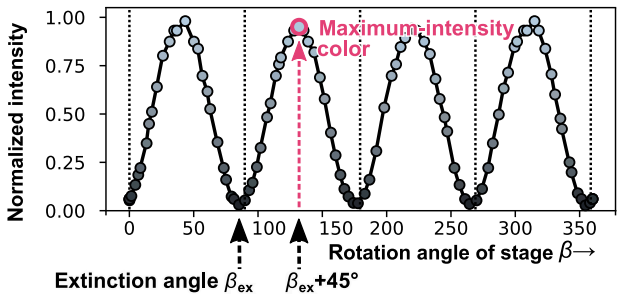


Figure 3 XPL grayscale intensity of a representative pixel as a function of stage angle. Intensity minima correspond to extinction, with maxima occurring ∼45° from extinction.

related to inclination and azimuth, respectively. To represent these two quantities in a unified form, we combine them into a single hue, saturation, and value (HSV) angle map (Fig. 5b, c, e, and f).

The HSV representation provides a compact encoding of azimuth- and inclination-related information and is convenient for image processing using standard libraries such as OpenCV (Bradski, 2000). Hue is naturally suited to the circular nature of the extinction angle, whereas value is used to represent an inclination-related quantity derived from the maximum intensity M_i.

For each pixel $i = (i_x, i_y)$, we define a normalized intensity contrast as

$$q_i = \mathrm{clip}\left(\frac{M_i - D_i}{M_{\mathrm{ref}} - D_i}, 0, 1\right), \tag{2}$$

where D_i is the intensity of the pixel i in D and M_{ref} is the 99.5th percentile of M over the field of view. For a uniaxial mineral, the retardation is calculated as

$$n_{\mathrm{eff}}(\theta) = \frac{n_{\mathrm{o}} n_{\mathrm{e}}}{\sqrt{n_{\mathrm{o}}^2 \sin^2\theta + n_{\mathrm{e}}^2 \cos^2\theta}}, R(\theta, t) = t\,|n_{\mathrm{eff}}(\theta) - n_{\mathrm{o}}| \tag{3}$$

where n_{o} and n_{e} are the ordinary and extraordinary refractive indices, t is the thin-section thickness, and θ is the angle between the c-axis and the thin-section normal.

The relation between recorded grayscale value and transmitted intensity depends on the camera and image-encoding pipeline. Standard sRGB uses a piecewise nonlinear transfer function rather than a pure square-root relation; however, calibration of the cellSens acquisition pipeline used here showed an effective response close to $I^{1/2}$ over the relevant intensity range. We therefore use this empirical approximation when constructing the segmentation proxy. Under XPL, $I \propto \sin^2(\pi R/\lambda)$, so the maximum-intensity value M_i scales approximately as $M_i \propto |\sin(\pi R/\lambda)|$ after this effective response is applied. In the low-retardation limit, $\pi R/\lambda \ll 1$, this relation reduces to $M_i \propto R$.

For $\Delta n/n_{\mathrm{o}} \ll 1$, where $\Delta n = n_{\mathrm{e}} - n_{\mathrm{o}}$, the first-order expansion of Equation (3) gives $R(\theta, t) \simeq R_{\max}\sin^2\theta$, where $R_{\max} = t|\Delta n|$ is the retardation at $\theta = 90°$. Accordingly, after subtraction of extinction brightness and normalization by Equation (2), q_i approximately follows $\sin^2\theta_i$. We therefore define the normalized inclination proxy as $\theta_i/(\pi/2) = (2/\pi)\arcsin\sqrt{q_i}$. The extinction angle and this inclination proxy are then encoded as hue and value, respectively:

$$H_i = \frac{\beta_{\mathrm{ex},i}}{90°}, S_i = 1, V_i = \frac{2}{\pi}\arcsin\sqrt{q_i}. \tag{4}$$

The resulting HSV angle map therefore combines the two orientation-sensitive quantities into a single image for subsequent grain segmentation.

HSV angle-map cleaning

The raw HSV angle map contains within-grain variations caused by impurities, surface contamination, scratches, and artifacts associated with finite thin-section thickness. Before grain segmentation, we therefore apply HSV image cleaning to reduce these variations while preserving discontinuities between grains.

The cleaning is based on the observation that these artifacts generally have lower V values than surrounding grain interiors. The algorithm enhances the contrast between high-V grain interiors and low-V features by propagating neighboring colors toward pixels with intermediate or locally reduced V. The detailed algorithm is described in Supplementary Section S1.3.

For each pixel with color $\mathbf{C}_i$, the colors of its eight neighboring pixels, $\mathbf{C}_j$, are examined. If a neighboring pixel has either a high V value or a very low V value, the selected neighbor $\mathbf{C}_{j*}$ is propagated toward the target pixel according to

$$\mathbf{C}_i^{(n+1)} = \frac{1}{2}\left\{\mathbf{C}_i^{(n)} + \mathbf{C}_{j*}^{(n)}\right\}, \tag{5}$$

where n denotes the iteration number. Repeated propagation makes the color within each grain more homogeneous, primarily by propagating colors from high-V pixels, while retaining very dark features. Excessive iteration can alter grains with intermediate V values;

Downloaded from academic.oup.com/petrology/article/67/11/egag099/9022254 by Hogaku-Bu Library user on 25 November 2026

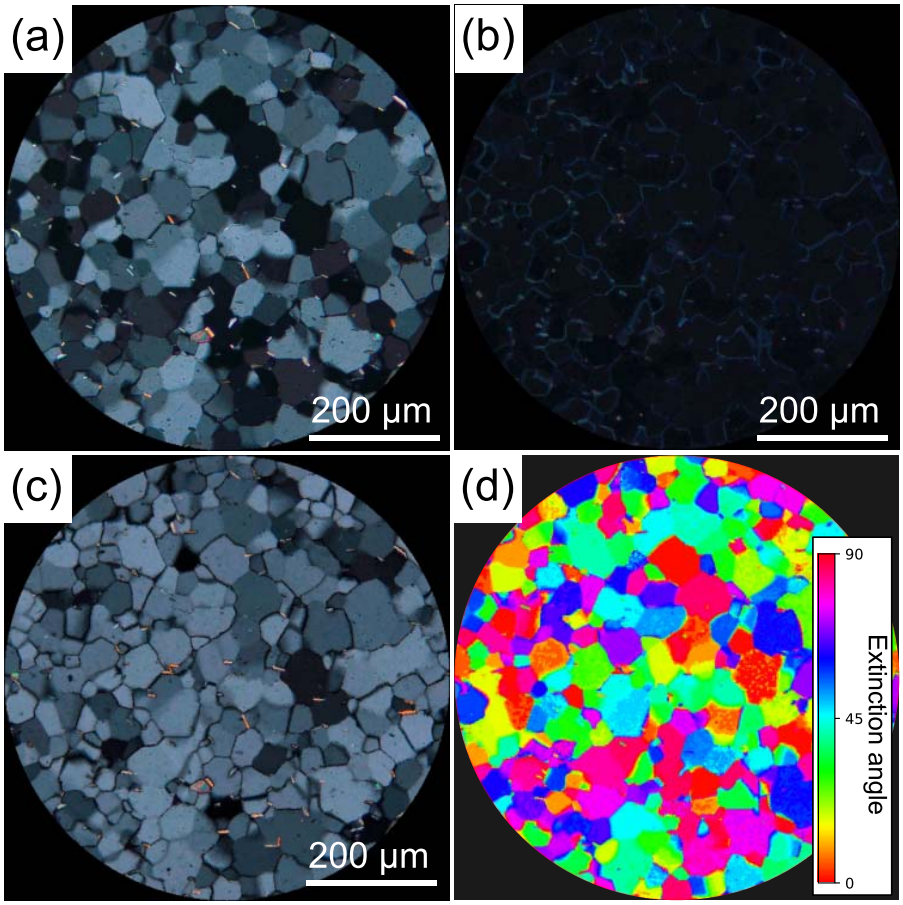


Figure 4 Quantities extracted from the XPL rotation sequence. (a) Raw image at the stage reference position. (b) Extinction-color map D, evaluated at β_{ex}. (c) Maximum-intensity image M, evaluated at $\beta_{ex} + 45°$. (d) Extinction-angle map B, with β_{ex} defined modulo $90°$.

empirically, ∼10 iterations suppressed unwanted variations without substantially modifying these grains.

The effect of the HSV image cleaning is shown in Fig. 5. For GGG3, within-grain variations in the original HSV angle map (Fig. 5b) are reduced after cleaning while grain-boundary features are preserved (Fig. 5c). The procedure is also effective for YM3 (Fig. 5e and f), despite stronger artifacts caused by impurities and scratches.

Orientation-based grain segmentation

The optical grain segmentation method uses differences in *c*-axis orientation, analogous to the misorientation criterion commonly used in EBSD. However, *c*-axis orientation represents only part of the full crystallographic orientation measured by EBSD. Therefore, even when the same angular threshold is applied, neighboring regions are more likely to be connected in the optical segmentation, and optically identified grains may therefore appear larger than EBSD grains. The optical and EBSD segmentation results are compared in the section *Accuracy and limitations of optical grain segmentation*.

The cleaned HSV angle map is first divided into superpixels using the Simple Linear Iterative Clustering with Zero Parameters algorithm (SLICO) (Fig. 6a; Achanta *et al.*, 2012). The segmentation strategy follows a similar approach to that of Jiang *et al.* (2018): the image is intentionally oversegmented into superpixels to preserve potential grain boundaries (Fig. 6b), and the resulting superpixels are subsequently merged based on orientation differences. The superpixel parameters used in this study are provided in Supplementary Section S1.4.

For each superpixel, a representative proxy orientation is calculated from the extinction angle β_{ex} and HSV value V. Here, V is converted to an inclination-related proxy as $\tilde{\theta} = 90°V$, where V is normalized to 0–1. For each pair of adjacent superpixels, the angular difference between their representative proxy orientations, each obtained as a circular median within the superpixel, is calculated. Adjacent superpixels are merged when this difference is smaller than the selected threshold; in this study, thresholds of 5°, 10°, and 15° were tested. The extinction-angle difference is evaluated modulo 90°.

This local merging criterion retains larger orientation discontinuities as grain boundaries. The boundaries after orientation-based merging are shown in Fig. 6c, and the resulting regions are displayed by their median colors in Fig. 6d.

Grain-boundary cleaning

Because HSV image cleaning preserves dark boundary-like features, elongated regions can remain between grains after orientation-based merging (Fig. 6d and e). These regions are not grains, and they are removed by a second cleaning step applied to the grain-label map, hereafter referred to as boundary cleaning.

For each region, we define the elongation index

Downloaded from academic.oup.com/petrology/article/67/11/egag099/9022254 by Hogaku-Bu Library user on 25 November 2026

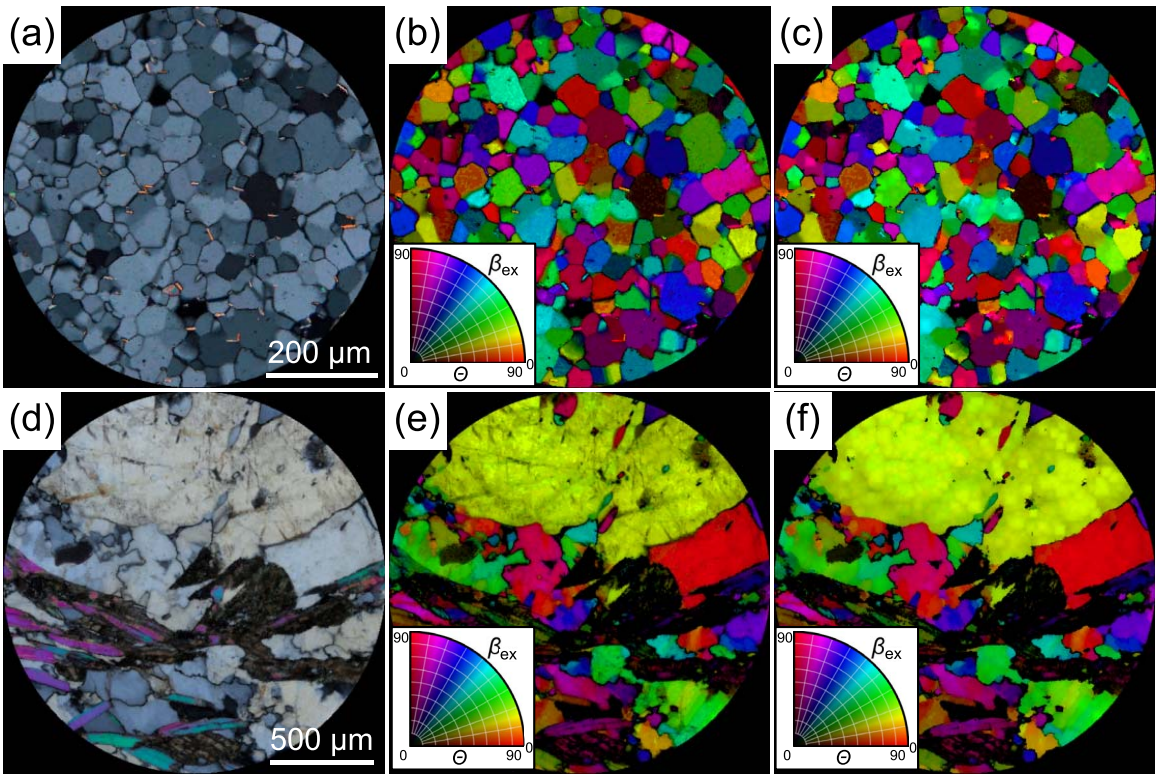


Figure 5 HSV angle maps for GGG3 and YM3. (a–c) GGG3: (a) maximum-intensity image, (b) HSV angle map constructed from the extinction angle and intensity-derived proxy, and (c) HSV angle map after HSV image cleaning by hue-constrained color propagation using Equation (5). (d–f) corresponding results for YM3. The HSV image cleaning suppresses artifacts caused by impurities and scratches in both samples.

$$\rho = \frac{L_{\mathrm{skel}}}{A}, \tag{6}$$

where A is the region area and L_{skel} is its skeleton length. For an elongated region of approximately uniform width w, ρ is approximately proportional to $1/w$, so regions satisfying

$$\rho \geq \frac{1}{w} \tag{7}$$

are narrower than about w. In this study, widths up to 5 pixels were treated as boundary-like features. The pixels of the identified regions are then reassigned to the nearest surrounding grain, so that no thin region remains between grains. The final grain-boundary map is shown in Fig. 6f.

Grain-size and grain-shape statistics

Grain size, shape, and grain-shape orientation provide complementary descriptors of grain-scale microstructure and are commonly used to characterize deformation-related fabrics (Xypolias, 2010; Ortolano *et al.*, 2020). Accordingly, NicoNavi quantifies three grain-scale geometric properties from the final grain-label map: grain size, aspect ratio, and major-axis orientation.

For each grain g, the grain area is denoted by A_g. Grain size is represented by the equivalent-area disc diameter (Pirard, 2004):

$$d_{\mathrm{eq},g} = 2\sqrt{\frac{A_g}{\pi}}. \tag{8}$$

Because the equivalent-area disc diameter is based only on area, it does not describe grain shape. A more detailed description of grain geometry is obtained from an equivalent ellipse. The aspect ratio and grain-shape orientation are determined from the second central moments of the grain region (Medalia, 1971). Let $L_{\mathrm{major},g}$ and $L_{\mathrm{minor},g}$ denote the major- and minor-axis lengths of this ellipse, respectively, and let ψ_g denote the orientation of its major axis. The aspect ratio is defined as

$$R_{\mathrm{asp},g} = \frac{L_{\mathrm{major},g}}{L_{\mathrm{minor},g}}, \quad L_{\mathrm{major},g} \geq L_{\mathrm{minor},g}. \tag{9}$$

The major-axis orientation ψ_g is an axial orientation with a period of 180°; therefore, the mean major-axis orientation is calculated using the standard doubled-angle treatment for axial data (Fisher, 1993). Each grain orientation is doubled and represented as a unit vector on the full 360° circle. The unit vectors are then averaged, and the resulting mean direction is divided by two to return the mean orientation to the 0–180° axial range.

Estimation of *c*-axis orientation

Azimuth

The extinction angle β_{ex} provides two possible azimuths separated by 90°. To distinguish these solutions, we use images acquired at +45° and −45° from extinction with a λ-plate (R_0 = 530 nm) inserted (Fig. 8a and b), and denote the color of pixel i in these images by $\mathbf{C}_i^+$

Downloaded from academic.oup.com/petrology/article/67/11/egag099/9022254 by Hogaku-Bu Library user on 25 November 2026

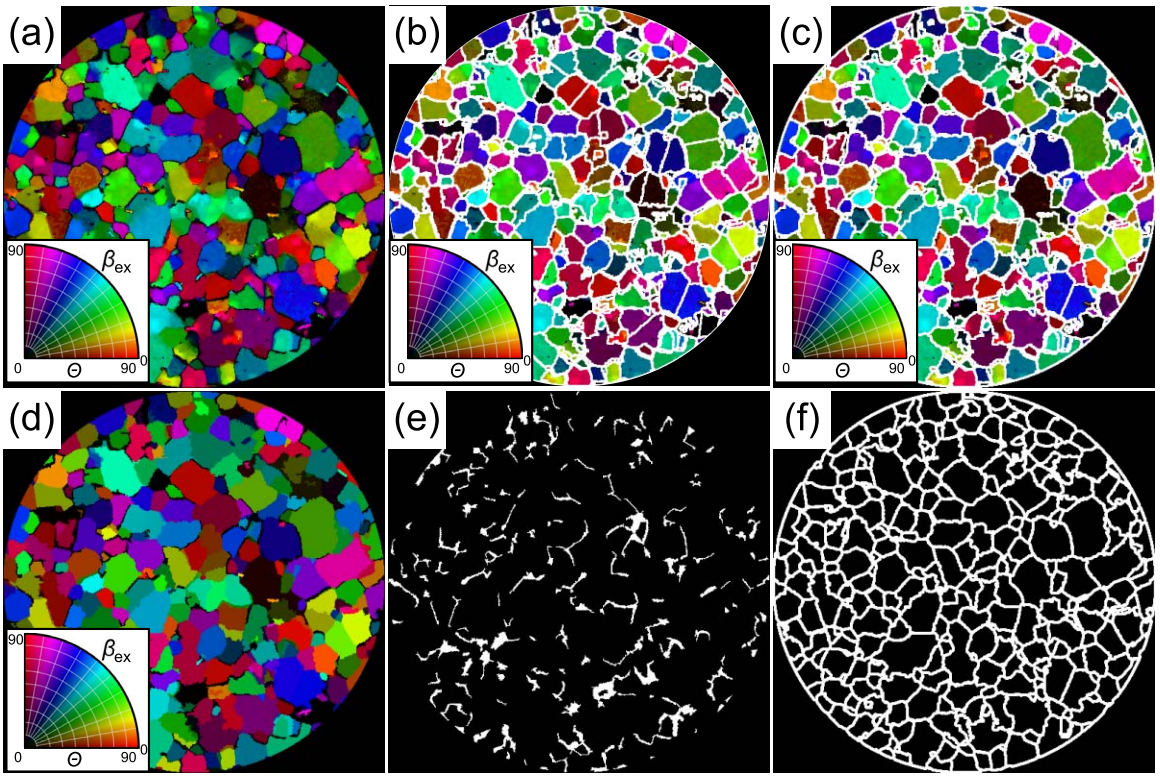


Figure 6 Grain-segmentation procedure. (a) Cleaned HSV angle map used for segmentation. (b) Initial superpixel oversegmentation. (c) Boundaries after orientation-based region merging. (d) Merged regions displayed using their median colors. (e) Thin, elongated regions identified by boundary cleaning. (f) Final grain-boundary map after boundary cleaning.

and $\mathbf{C}_i^-$. Both colors are evaluated with a single color-fitting procedure. Combined with the color model in Supplementary Section S1.5, the retardation relation in Equation (3) provides a theoretical color $\mathbf{c}(\theta)$ for each inclination θ. Here, the coordinate system for azimuth φ and inclination θ follows the optical-microscope field of view, in which the north–south and east–west directions are reversed relative to the sample (Fig. 7).

An observed color $\mathbf{y}$ is then modeled as

$$\mathbf{y} \approx \alpha \mathbf{c}(\theta), \tag{10}$$

where α is a single brightness scale accounting for uniform darkening by optical components and mineral absorption. The parameters θ and α are estimated by alternating optimization of color residuals, with a robust loss used to reduce the influence of outliers (Supplementary Section S1.6). The fit is applied pixel by pixel to $\mathbf{C}_i^+$ and $\mathbf{C}_i^-$, with one α fitted jointly to both images; for GGG3, $\alpha = 0.762$. The two colors yield apparent inclinations $\theta_i^{\pm}$, which are converted to mineral retardations $R_i^{\pm}$ using Equation (3). The resulting R^+ and R^- maps are shown in Fig. 8c and d. The configuration with the larger retardation is identified as additive and determines which azimuth candidate is selected (Fig. 8e).

The azimuth φ_i is then calculated from the extinction angle as

$$\varphi_i = \begin{cases} \left(180^\circ - \beta_{\mathrm{ex},i}\right) \bmod 180^\circ, & R_i^+ \geq R_i^-, \\ \left(90^\circ - \beta_{\mathrm{ex},i}\right) \bmod 180^\circ, & R_i^+ < R_i^-. \end{cases} \tag{11}$$

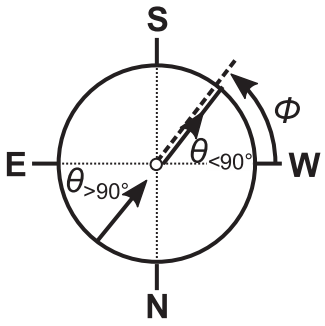


Figure 7 Microscope-view coordinate system used to define azimuth φ and inclination θ.

The resulting azimuth map is shown in Fig. 8f. Here, φ is defined over 0–180° and represents the orientation of the *c*-axis projected onto the thin-section plane. The remaining ambiguity between the two inclination branches is resolved using the stage-tilt procedure described in the section *Resolving the inclination ambiguity by stage tilt*.

Inclination magnitude

Previous optical methods estimated inclination using circularly polarized images (Heilbronner & Barrett, 2014), which are optically analogous to the maximum-intensity images obtained during stage rotation. In both cases, the signal is independent of azimuth and decreases in intensity as the *c*-axis approaches the thin-section normal. However, low interference-color intensity may also result from absorption by

Downloaded from academic.oup.com/petrology/article/67/11/egag099/9022254 by Hogaku-Bu Library user on 25 November 2026

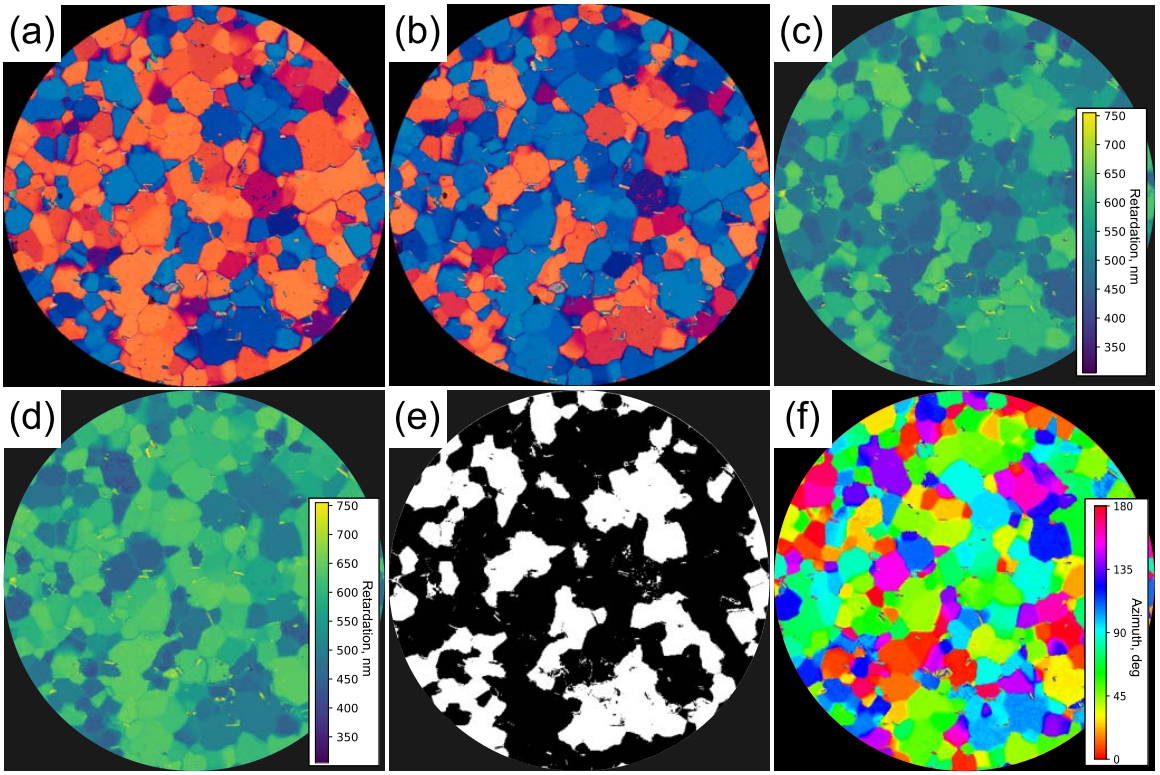


Figure 8 Determination of azimuth. (a and b) images acquired at $+45°$ and $-45°$ from extinction with the λ-plate inserted. (c and d) corresponding retardation maps, R^+ and R^-, obtained by color fitting. (e) Additive/subtractive branch determined by comparing R^+ and R^-. (f) Resulting azimuth φ over 0–180°.

optical components or variations in camera response, making these effects difficult to distinguish from inclination-related variations.

We therefore estimate inclination from the additive image ($\mathbf{C}_{\mathrm{add}}$; Fig. 9a) constructed from the two λ-plate images acquired at +45° and −45° from extinction. For each pixel, the image with the larger retardation is selected:

$$\mathbf{C}_{\mathrm{add},i} = \begin{cases} \mathbf{C}_i^+, & R_i^+ \geq R_i^-, \\ \mathbf{C}_i^-, & R_i^+ < R_i^-. \end{cases} \tag{12}$$

Unlike the maximum-intensity image, whose color approaches black at low retardation, the additive image follows a vivid color sequence from purple to blue as the *c*-axis changes from nearly parallel to the thin-section normal toward the thin-section plane. Inclination is therefore expressed mainly as a change in chromaticity rather than brightness, helping separate the crystallographic signal from optical-system and acquisition effects.

The inclination is then obtained from the additive image by color fitting with Equations (3) and (10), as detailed in Supplementary Section S1.6. For each grain g, the observed additive color $\mathbf{y}_g$ is sampled from the grain center to minimize mixed-color effects at grain boundaries, and the inclination θ_g is estimated together with a single brightness factor α_{add} shared by all grains. For GGG3, $\alpha_{\mathrm{add}} = 0.731$. Because the additive configuration has already been selected in Equation (12), the fitted θ_g is the inclination of the grain itself.

The thickness t substituted into Equation (3) is the measured thin-section thickness. However, a thin adhesive layer is commonly present between the thin section and the glass slide, so this value may overestimate the true mineral thickness. We therefore refine θ by assuming that the highest-retardation grains have *c*-axes close to the thin-section plane and by using the 95th percentile of the fitted inclination distribution, $\theta_{\max}$, to correct this systematic bias (Fig. 9b):

$$\theta_g^{\mathrm{corr}} = \arcsin\left[\min\left(\frac{\sin\,\theta_g}{\sin\,\theta_{\max}}, 1\right)\right]. \tag{13}$$

This correction rescales the upper end of the inclination distribution to 90° (Fig. 9b), and the corresponding maps are shown in Fig. 9c and d.

Resolving the inclination ambiguity by stage tilt

The interference color constrains the magnitude of the inclination but cannot distinguish between θ and 180° − θ. We resolve this ambiguity by introducing a small stage tilt. The two candidate *c*-axis orientations respond differently to tilting because their angles relative to the thin-section normal change in opposite ways. Consequently, they produce different changes in interference color. We therefore determine the inclination branch by comparing the observed color change with the changes predicted for the two candidates.

Heilbronner & Barrett (2014) compared intensity changes using the red channel or bandpass-filtered images. The present method instead calibrates full RGB colors with a regression model before comparing observed and predicted color changes. A stage tilt of ∼7° can be introduced either by placing a thin plate beneath one side of the thin section or by using a dedicated 3D-printable tilting stage (Fig. 10).

Figure 11a and b show the measured interference colors before and after tilting. Because tilting the thin section shifts the focal plane across the field of view, the tilted image was reconstructed by focus stacking

Downloaded from academic.oup.com/petrology/article/67/11/egag099/9022254 by Hogaku-Bu Library user on 25 November 2026

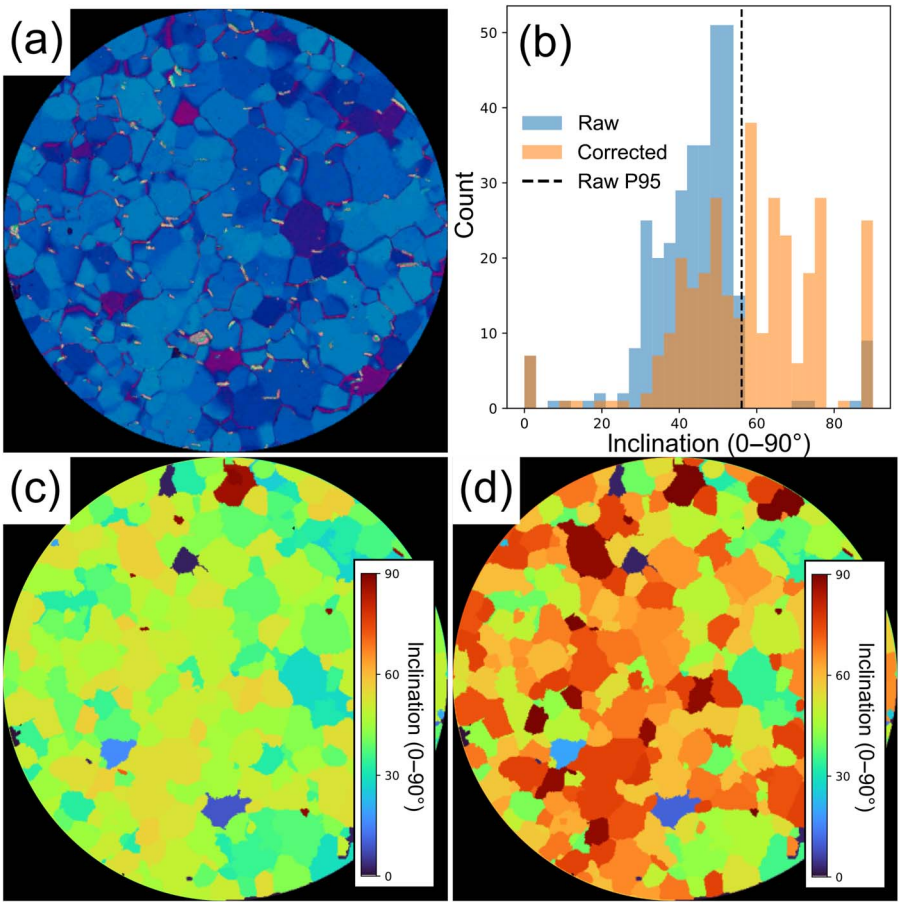


Figure 9 Estimation of inclination magnitude. (a) Additive image constructed from the $+45°$ and $-45°$ λ-plate images. (b) Inclination distributions before and after correction, with the 95th percentile value θ_{max} indicated. (c) Inclination map before correction. (d) Inclination map after correction.

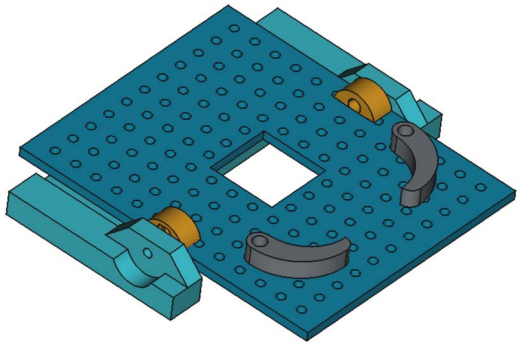


Figure 10 A 3D-printable tilting stage used to introduce a small stage tilt.

a focus-sweep video (Supplementary Section S1.7). The untilted and tilted images were then spatially aligned using phase-only correlation (Reddy & Chatterji, 1996). After alignment, a constant offset was added to the HSV V channel of the tilted image so that its median within the shared valid region matched that of the untilted image, following the image-intensity normalization approach of Heilbronner & Barrett (2014).

The observed RGB color change between the registered images is shown in Fig. 11c. Before predicting this change, the theoretical color model was calibrated against the measured colors in the untilted image. For each grain g, the pixel at the grain centroid was used, and the theoretical color $\mathbf{c}_g(\varphi_g, \theta_g)$ was calculated from its azimuth φ_g and inclination θ_g using the Jones color model (Supplementary Section S1.5). The measured color $\mathbf{y}_g$ was related to the theoretical color by

$$\mathbf{y}_g \approx \alpha_{color} M \mathbf{c}_g(\varphi_g, \theta_g) + \mathbf{b}, \mathrm{tr}(M) = 3 \tag{14}$$

where α_{color} is a scalar brightness factor, M is a 3×3 color-correction matrix, and $\mathbf{b}$ is an RGB offset. This extends Equation (10); the more flexible correction is used because measured color depends on azimuth and the color change caused by the small stage tilt is relatively weak. The fitting was initialized with $M = I$ and $\mathbf{b} = \mathbf{0}$, then refined by alternately estimating $(M, \mathbf{b})$ and α_{color} (Supplementary Section S1.8). For the GGG3 example, fitting 300 grains gave

$$\alpha_{color} = 0.885, \quad M = \begin{pmatrix} 1.17 & 0.03 & -0.12 \\ -0.04 & 0.92 & 0.06 \\ 0.12 & 0.01 & 0.91 \end{pmatrix}, \mathbf{b} = \begin{pmatrix} 22.4 \\ -3.3 \\ 10.6 \end{pmatrix}. \tag{15}$$

The calibrated model was then used to predict the color change caused by tilting for the two possible inclination branches. For each inclination magnitude obtained as described above, the two candidates θ and $180° - \theta$ were evaluated separately. The predicted RGB changes for the $\theta < 90°$ and $\theta > 90°$ candidates are shown in Fig. 11d and e. Finally,

Downloaded from academic.oup.com/petrology/article/67/11/egag099/9022254 by Hogaku-Bu Library user on 25 November 2026

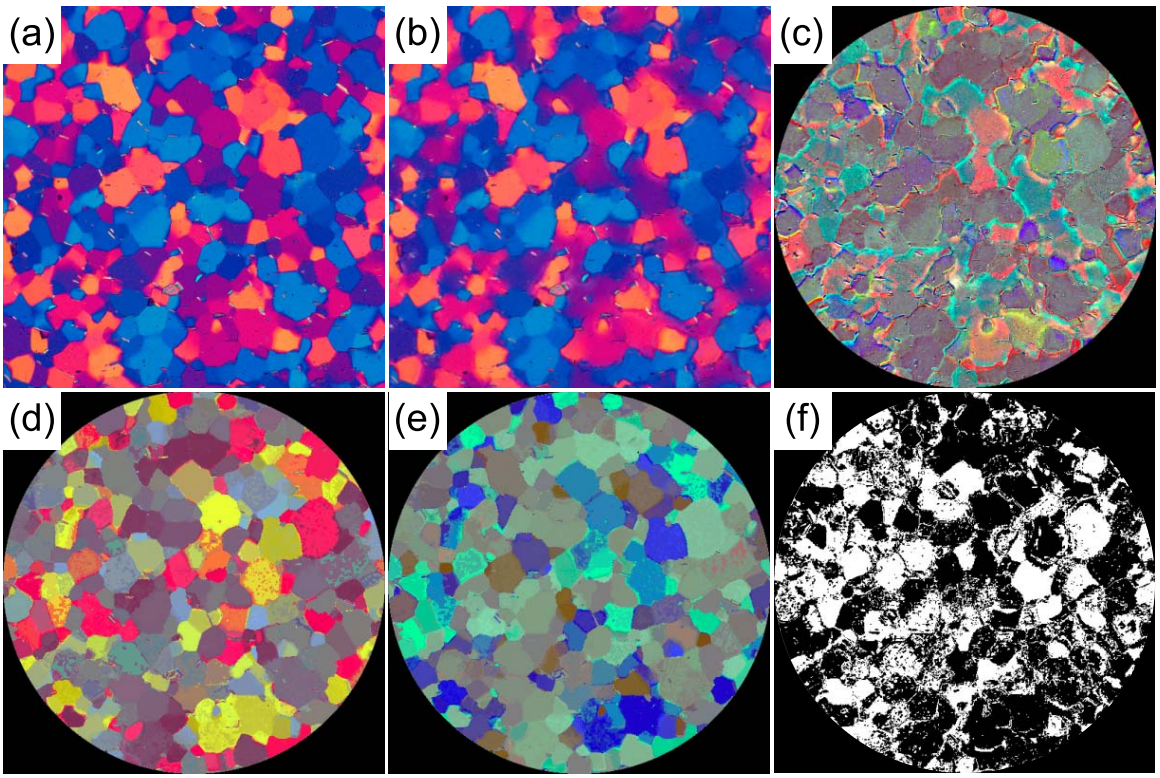


Figure 11 Resolving the inclination ambiguity by stage tilt, illustrated at the 45° stage position. (a and b) measured colors before and after tilting. (c) Observed RGB color change, amplified and centered on mid-gray for visualization. (d and e) predicted color changes for the $\theta < 90^\circ$ and $\theta > 90^\circ$ candidates, respectively. (f) Selected inclination branch; white indicates $\theta > 90^\circ$.

the observed RGB-change vector (Fig. 11c) was compared with both predicted vectors using cosine similarity, and the candidate with the higher similarity was selected. The resulting branch selection is shown in Fig. 11f, where white indicates grains assigned to $\theta > 90^\circ$.

To improve the robustness of this selection, the same measurements were performed at stage positions of 0° and 45°. At the 0° stage position, grains with azimuths near 0° or 180° show essentially no color change upon tilting, making the branch selection unreliable. The 45° stage position was therefore used for grains with $\varphi < 30^\circ$ or $\varphi > 150^\circ$, whereas the 0° data were used for the remaining grains.

Semi-supervised mineral classification

Grain segmentation defines individual grains but does not identify their minerals. We use semi-supervised classification to extend a limited number of user annotations to the remaining segmented grains.

Each grain is represented by five features describing shape, size, and interference color. The shape and size features are the logarithm of the aspect ratio and the logarithm of grain area, respectively; the color features are the median L^*, a^*, and b^* values in the CIE 1976 $L^*a^*b^*$ (CIELAB) color space of the maximum-intensity image. Thus, for N segmented grains, the classification uses an $N \times 5$ feature matrix. Definitions of these features and details of the classification procedure are given in Supplementary Section S1.9.

The user manually assigns mineral classes to a limited number of representative grains. The remaining grains are classified using feature-space similarity to labeled grains and graph-based label propagation implemented with scikit-learn LabelPropagation (Zhu & Ghahramani, 2002). The classification is recalculated as new labels are added, allowing interactive refinement. This iterative strategy focuses manual labeling on grains that remain misclassified under the current prediction. Labeling is continued until the classification is judged satisfactory by the user. Thus, the choice of labeling strategy primarily affects how efficiently the desired classification is reached, rather than the final classification itself.

An example for the YM3 sample is shown in Fig. 12. The grains were divided into three user-defined classes: mainly quartz, mica, and other, with the last class mainly representing fine-grained mineral aggregates. As the number of labeled grains increased from 5 to 70 (Fig. 12b–d), the classification became progressively more consistent with visual interpretation; in this example, 70 labels produced a classification judged visually reasonable by the user over this field of view.

Because the classification relies on user-defined labels derived from optical images, it cannot reliably distinguish minerals that have similar optical appearances. For example, quartz and feldspar may require additional information for reliable classification.

Results and discussion

Here, we evaluate the accuracy and limitations of optical grain segmentation and *c*-axis orientation estimation by comparison with EBSD data. Throughout these comparisons, optical segmentation used 10 HSV angle-map cleaning iterations and a 5-pixel width threshold for grain-boundary cleaning. Grain-boundary segmentation thresholds of 5°, 10°, and 15° were tested and compared with EBSD grain boundaries constructed using the same misorientation thresholds.

Downloaded from academic.oup.com/petrology/article/67/11/egag099/9022254 by Hogaku-Bu Library user on 25 November 2026

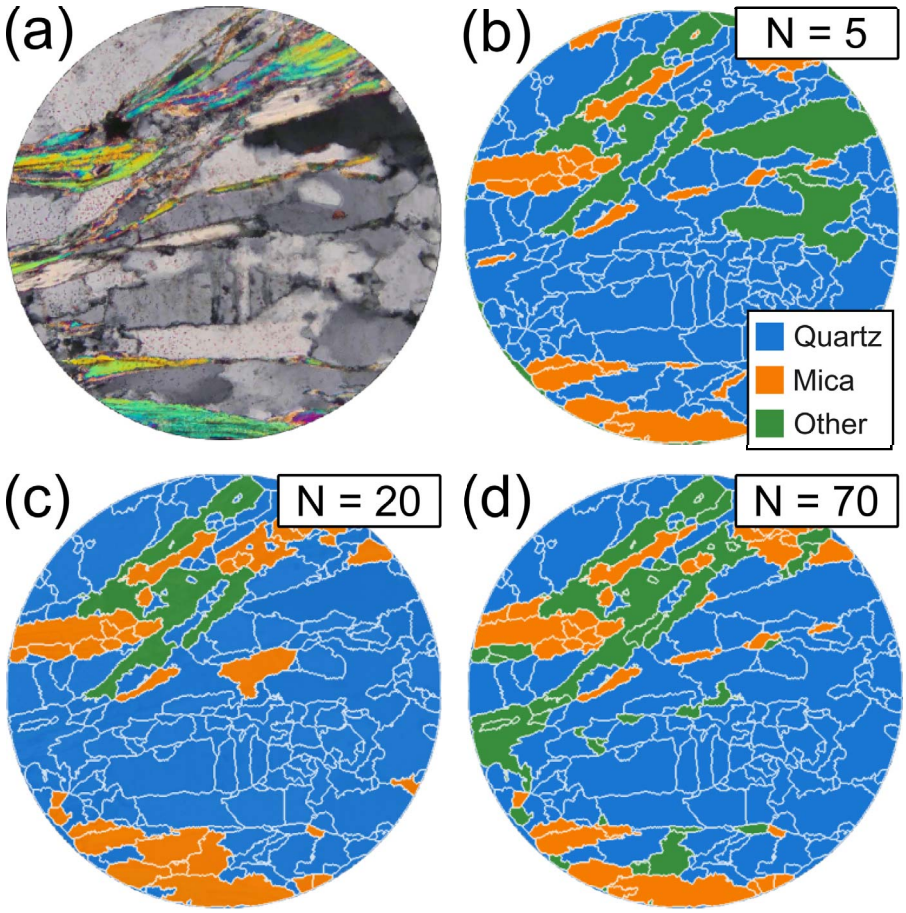


Figure 12 Semi-supervised mineral classification of the YM3 sample. (a) Maximum-intensity image. (b–d) Classification maps obtained using 5, 20, and 70 manually labeled grains, respectively. The classification results distinguish three categories: mainly quartz, mica, and other.

Accuracy and limitations of optical grain segmentation

We first evaluate how well optical segmentation reproduces grain boundaries identified by EBSD. Figure 13 compares the relatively thin GGG3 sample (22 μm) and the thicker GGG2 sample (45 μm). An optical boundary and an EBSD boundary were regarded as matching when their positions agreed within ±1% of the image width. Here, an unmatched boundary plotted in red in the optical result represents a false boundary, whereas an unmatched EBSD boundary represents a boundary missed by the optical segmentation.

For GGG3, optical and EBSD grain boundaries show generally good agreement when a 5° threshold is used (Fig. 13c and d). In contrast, more false and missed boundaries occur in the thicker GGG2 sample (Fig. 13e and f). One characteristic error in GGG2 is the occurrence of two approximately parallel boundaries along a single grain contact. Because a boundary is observed through a thin section of finite thickness, its optical expression can appear as a broad band rather than a narrow line, causing the segmentation to identify the two sides of the band as separate boundaries. This error becomes more pronounced as thin-section thickness increases and is difficult to remove simply by adjusting the parameters; reducing thin-section thickness is therefore the most direct way to suppress it. The comparison for GGG3 further shows that increasing the threshold from 5° to 15° results in more missed boundaries (Fig. 13g and h). This indicates that a larger threshold promotes merging of neighboring grains with relatively small differences in *c*-axis orientation, thereby removing boundaries that remain distinct in the EBSD segmentation.

The same trends with thin-section thickness and segmentation threshold are observed across all five GGG samples (Fig. 14). Both error rates generally increase with thin-section thickness. With increasing segmentation threshold, missed-boundary rates increase, whereas false-boundary rates generally decrease slightly or remain similar. Under most tested conditions, missed-boundary error rates are higher than false-boundary error rates.

This tendency reflects a fundamental difference between optical and EBSD boundary definitions. EBSD segmentation is based on full crystallographic misorientation between adjacent regions, including rotation around the *c*-axis. In contrast, the optical segmentation used here is based on differences in optically estimated *c*-axis orientation. Adjacent grains can therefore have similar *c*-axis orientations while still having a crystallographic misorientation detectable by EBSD, and such boundaries are likely to be missed optically. Increasing the threshold angle further promotes merging across these relatively small optical orientation differences.

Thin-section thickness alone, however, does not determine whether grain boundaries can be recovered optically. W1415 provides an example of substantial segmentation failure despite its relatively small thickness of 25 μm (Fig. 15). The upper middle part of this sample contains many grains with *c*-axes close to the thin-section normal ($\theta \sim 0°$). These grains appear very dark even in the maximum-intensity

Downloaded from academic.oup.com/petrology/article/67/11/egag099/9022254 by Hogaku-Bu Library user on 25 November 2026

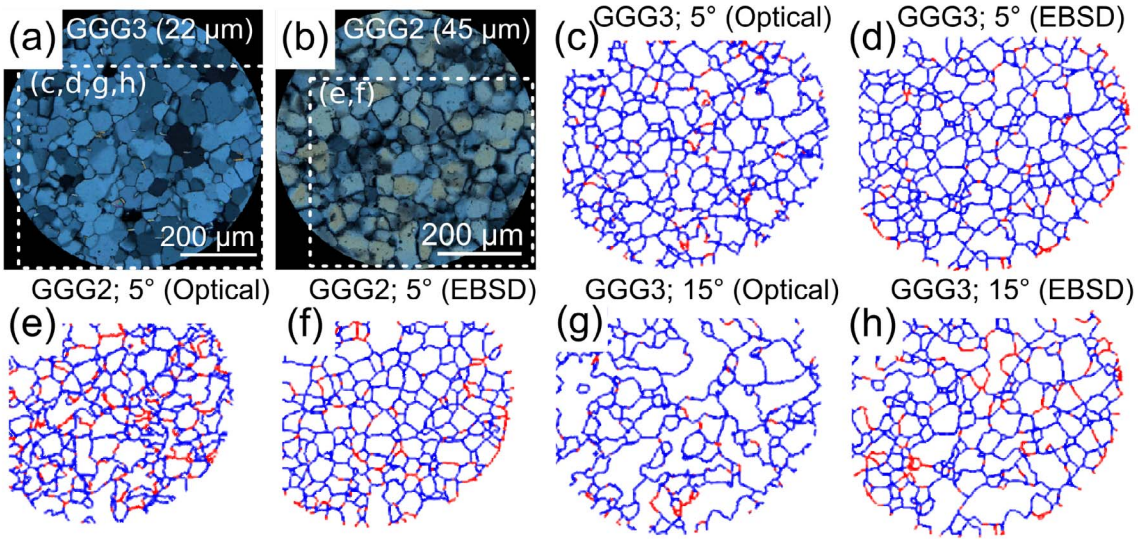


Figure 13 Comparison of optically and EBSD-derived grain boundaries. (a and b) maximum-intensity images of GGG3 (22 μm) and GGG2 (45 μm), respectively. (c and d) optical and EBSD grain boundaries for GGG3 using a 5° threshold. (e and f) corresponding results for GGG2 using a 5° threshold. (g and h) corresponding results for GGG3 using a 15° threshold. Boundary segments are classified as matched when a corresponding boundary is found within ±1% of the image width, and as unmatched otherwise.

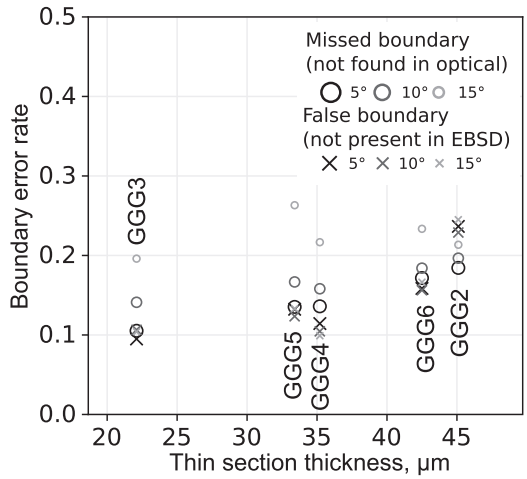


Figure 14 Grain-boundary error rates for GGG2–GGG6 as a function of thin-section thickness. Circles indicate missed-boundary rates and crosses indicate false-boundary rates for segmentation thresholds of 5°, 10°, and 15°.

image, so the maximum-intensity and extinction-angle information used for segmentation provides little contrast between neighboring grains. Consequently, many boundaries that are clearly distinguished by EBSD are not recovered optically.

Thus, reliable optical grain segmentation requires not only a sufficiently thin section and an appropriately small segmentation threshold, but also sufficient optical contrast between neighboring grains. In particular, grain populations whose c-axes are close to the microscope axis can remain difficult to distinguish even in relatively thin sections.

Effects of segmentation on grain-scale statistics

The segmentation differences described above also affect quantities calculated from segmented grains. We therefore compared three representative grain-scale properties derived from the optical and EBSD segmentations: the number of grains, the mean grain-shape orientation, and the mean grain aspect ratio (Fig. 16). Grains are equally weighted in the mean grain-shape orientation and mean aspect-ratio calculations.

The number of optically segmented grains is systematically smaller than the number obtained from EBSD (Fig. 16a). This difference is consistent with the predominance of missed boundaries shown in Fig. 14. For the thinner GGG samples, particularly with a 5° threshold, optical grain counts are closer to EBSD values.

The mean grain-shape orientation was also compared between optical and EBSD segmentations (Fig. 16b). Except for GGG5, optical estimates generally fall within ∼±20° of EBSD values and show no clear dependence on threshold or thin-section thickness. GGG5 shows a larger discrepancy because it has little preferred grain-shape orientation, so its mean orientation is poorly constrained (Supplementary Section S2.4).

The mean grain aspect ratio shows a clearer dependence on segmentation quality (Fig. 16c). For the thinner GGG samples and a 5° threshold, optical estimates are relatively close to those obtained from EBSD.

W1415 illustrates how selective segmentation failure can bias grain-shape statistics. As discussed above, many grains in this sample have c-axes nearly normal to the thin-section plane and are therefore difficult to distinguish optically. As a result, the number of grains is underestimated in the optical segmentation (Fig. 16a). In the EBSD segmentation, grains that are difficult to distinguish optically tend to have relatively low aspect ratios. Their preferential omission therefore shifts the optically identified grain population toward more elongated grains, resulting in higher estimated aspect ratios (Fig. 16c).

Accuracy and limitations of optical *c*-axis orientation estimates

We next evaluate how accurately the optical method reproduces *c*-axis orientations and how errors in individual estimates affect pole figures. Figure 17 compares the azimuth and inclination of individual

Downloaded from academic.oup.com/petrology/article/67/11/egag099/9022254 by Hogaku-Bu Library user on 25 November 2026

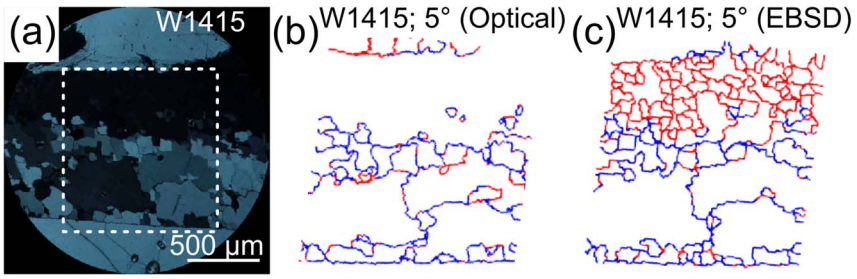


Figure 15 Example of grain segmentation for W1415 using a 5° threshold. (a) Maximum-intensity image. (b) Optically derived grain boundaries. (c) EBSD-derived grain boundaries. Boundary segments are classified as matched when a corresponding boundary is found within ±1% of the image width, and as unmatched otherwise.

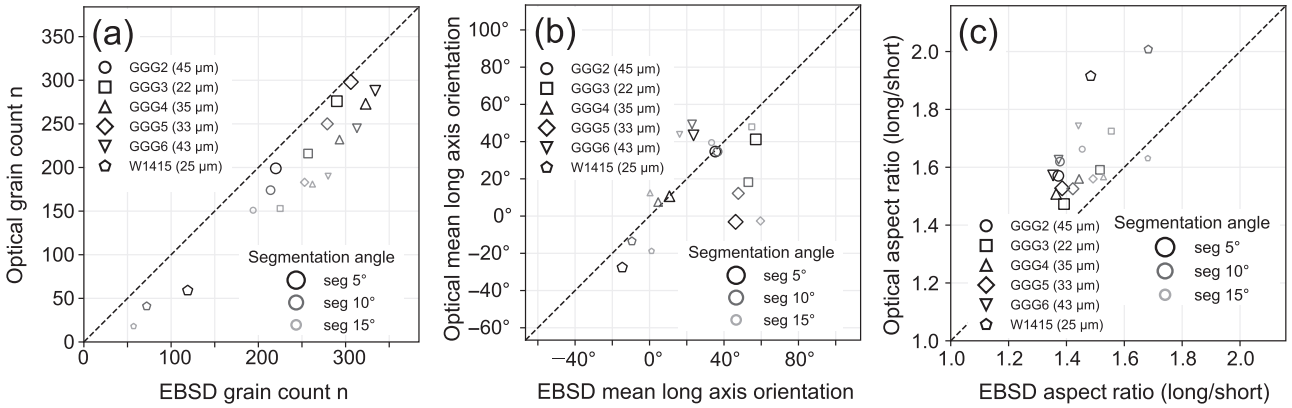


Figure 16 Comparison of grain-scale properties derived from optical and EBSD grain segmentation. (a) Number of segmented grains, (b) mean grain-shape orientation, and (c) mean grain aspect ratio. Grains are equally weighted in the mean orientation and aspect-ratio calculations. Symbol shapes indicate samples, and symbol shades indicate segmentation thresholds of 5°, 10°, and 15°. Dashed lines show the 1:1 relation.

grains with EBSD results, using a 5° segmentation threshold. An optical grain and an EBSD grain were treated as the same grain when their overlap exceeded 50% of the larger grain area, and azimuth and inclination at the grain center were compared. For the relatively thin GGG3 sample (22 μm), most grains plot close to the 1:1 line (Fig. 17a and b), indicating that the optical method generally reproduces the *c*-axis orientations of successfully segmented grains.

A small number of GGG3 grains nevertheless show large inclination errors. The points marked A in Fig. 17b lie approximately along the relation between θ and 180° − θ. These errors result from incorrect selection between the two possible inclination directions during stage-tilt analysis, and about 7% of grains in this sample are assigned to the wrong inclination branch. The same incorrect selection remains at or below about 7% in the thinner samples (GGG3, GGG4, and GGG5), whereas the corresponding rates in the thicker samples (GGG2 and GGG6) exceed 10%. Per-sample comparisons are provided in Supplementary Section S2.1.

The thicker GGG2 sample (45 μm) shows greater scatter in both azimuth and inclination (Fig. 17c and d). In particular, several systematic misinterpretations occur in the inclination estimates. The points marked B in Fig. 17d show a wide range of EBSD inclinations but optical inclinations concentrated near 50° and 130°.

This concentration reflects the sensitivity of RGB color to retardation. In the additive image, inclination estimates are biased at retardations of approximately $R_0 + \left(116\text{–}167\ \mathrm{nm}\right)$ because the interference color is relatively insensitive to changes in inclination. In this range, changes in inclination produce only small variations in the red and blue channels because their intensities are close to saturation. As a result, a range of true inclinations can be represented by very similar colors and therefore assigned similar optical inclinations.

The concentration marked C in Fig. 17d has a different origin. Several grains are assigned an inclination of exactly 90° because the correction in Equation (13) rescales the fitted distribution using its 95th percentile and clips values above this reference at 90°. Some accumulation at 90° is therefore expected from the correction itself. A similar artificial accumulation can occur at 0° when the measured RGB color falls outside the modeled inclination range. Therefore, a strong concentration exactly at 0° or 90° should not automatically be interpreted as a crystallographic preferred orientation.

These grain-by-grain errors can be evaluated more directly through their effect on *c*-axis pole figures (Fig. 18). We constructed pole figures in two ways. In the grain-based approach, each segmented grain contributes one representative orientation, calculated from the median orientation within that grain. In the pixel-based approach, orientations are sampled directly from 10 000 randomly selected pixels without using grain segmentation. The former gives approximately equal weight to individual grains, whereas the latter represents the spatial distribution of orientations independently of whether boundaries are correctly recovered. Corresponding results for all samples are provided in Supplementary Sections S2.2 and S2.3.

For GGG3, both grain-based and pixel-based optical pole figures reproduce the main orientation distribution observed by EBSD (Fig. 18a and b). This is consistent with the grain-by-grain comparison in Fig. 17a and b: the relatively thin section allows both grain boundaries and within-grain orientations to be estimated with comparatively small errors. The similarity between the grain-based

Downloaded from academic.oup.com/petrology/article/67/11/egag099/9022254 by Hogaku-Bu Library user on 25 November 2026

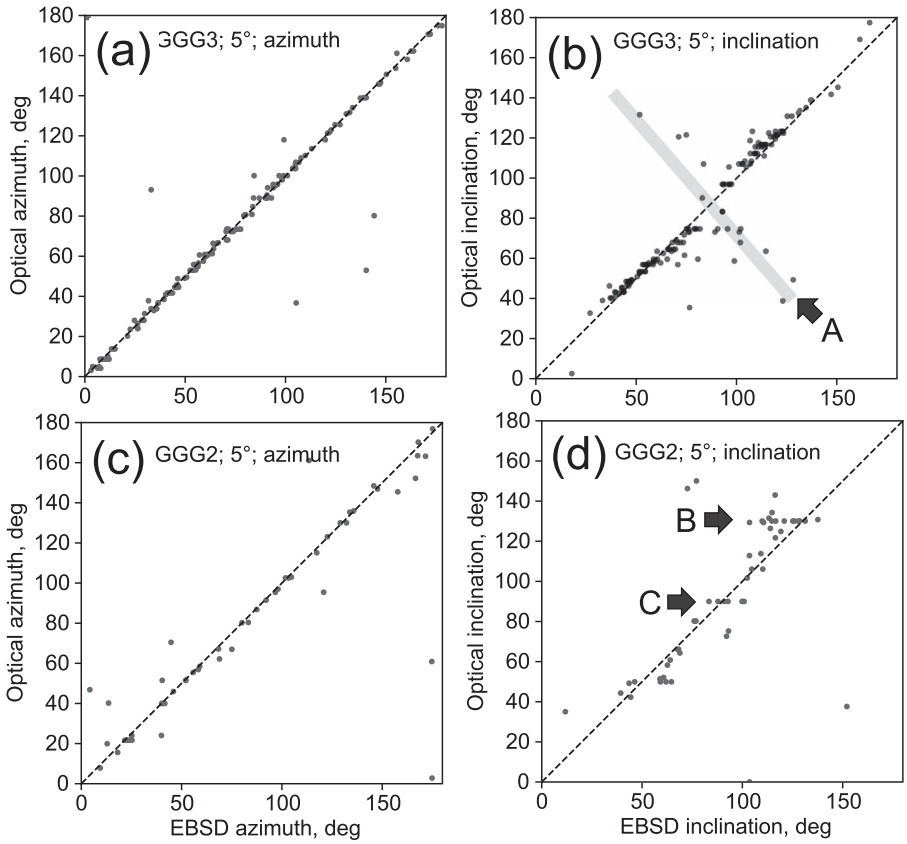


Figure 17 Comparison of *c*-axis orientations estimated optically and by EBSD using a 5° grain-segmentation threshold. (a, b) azimuth and inclination, respectively, for GGG3 (22 μm). (c, d) corresponding results for GGG2 (45 μm). Dashed lines indicate the 1:1 relation. Labels A–C indicate features discussed in the text.

and pixel-based results also indicates that segmentation does not strongly bias the overall fabric in this sample.

In the thicker GGG2 sample, optical pole figures show a stronger concentration along a limited inclination range than the EBSD results (Fig. 18c and d). This feature corresponds to the inclination concentration marked B in Fig. 17d. Because the interference color is relatively insensitive to retardation within the interval described above, orientations with different true inclinations can be mapped to similar optical inclinations.

W1415 shows a different type of discrepancy (Fig. 18e and f). As discussed in the section *Accuracy and limitations of optical grain segmentation*, W1415 contains many grains with c-axes close to the thin-section normal. These dark, low-contrast regions are merged into a small number of optical grains. In the grain-based pole figure, each merged region contributes only one representative orientation, so the strong EBSD concentration near the thin-section normal is greatly reduced in the optical result (Fig. 18e). In contrast, the pixel-based optical pole figure retains a central concentration more similar to the EBSD distribution (Fig. 18f), because pixels with these orientations are counted even when individual grain boundaries are not identified.

The comparison of the two pole-figure approaches therefore helps distinguish two sources of uncertainty. Pixel-based analysis can reduce biases caused by segmentation failure, as illustrated by W1415, but it cannot correct systematic errors in the estimated orientation itself, such as the insensitive retardation range observed for GGG2. Grain-based pole figures are appropriate when individual grains are reliably segmented. When segmentation is unreliable, however, a pixel-based comparison provides a useful complementary representation of the orientation distribution.

Practical implications and recommendations

Overall, the optical analysis provides *c*-axis orientation and grain-scale information that are broadly consistent with EBSD when thin sections are sufficiently thin and grain boundaries have adequate optical contrast. Among the conditions tested here, a 5° segmentation threshold and a thin-section thickness of ∼20–35 μm gave the most reliable grain segmentation and grain-based measurements. Greater thin-section thicknesses increase boundary-detection errors, whereas some grain populations remain difficult to segment even in thin sections when neighboring grains have similar optical responses.

Orientation analysis is affected not only by grain segmentation but also by the optical sensitivity of the retardation measurement. In particular, systematic concentrations caused by insensitive retardation ranges or inclination correction should be distinguished from true crystallographic preferred orientations. With these limitations considered, the method provides a practical approach for quantitative *c*-axis analysis from polarized-light microscopy without requiring EBSD measurements.

Integrated NicoNavi workflow and applications

The analyses described above are integrated in NicoNavi, a Python-based application that provides a graphical interface for step-by-step

Downloaded from academic.oup.com/petrology/article/67/11/egag099/9022254 by Hogaku-Bu Library user on 25 November 2026

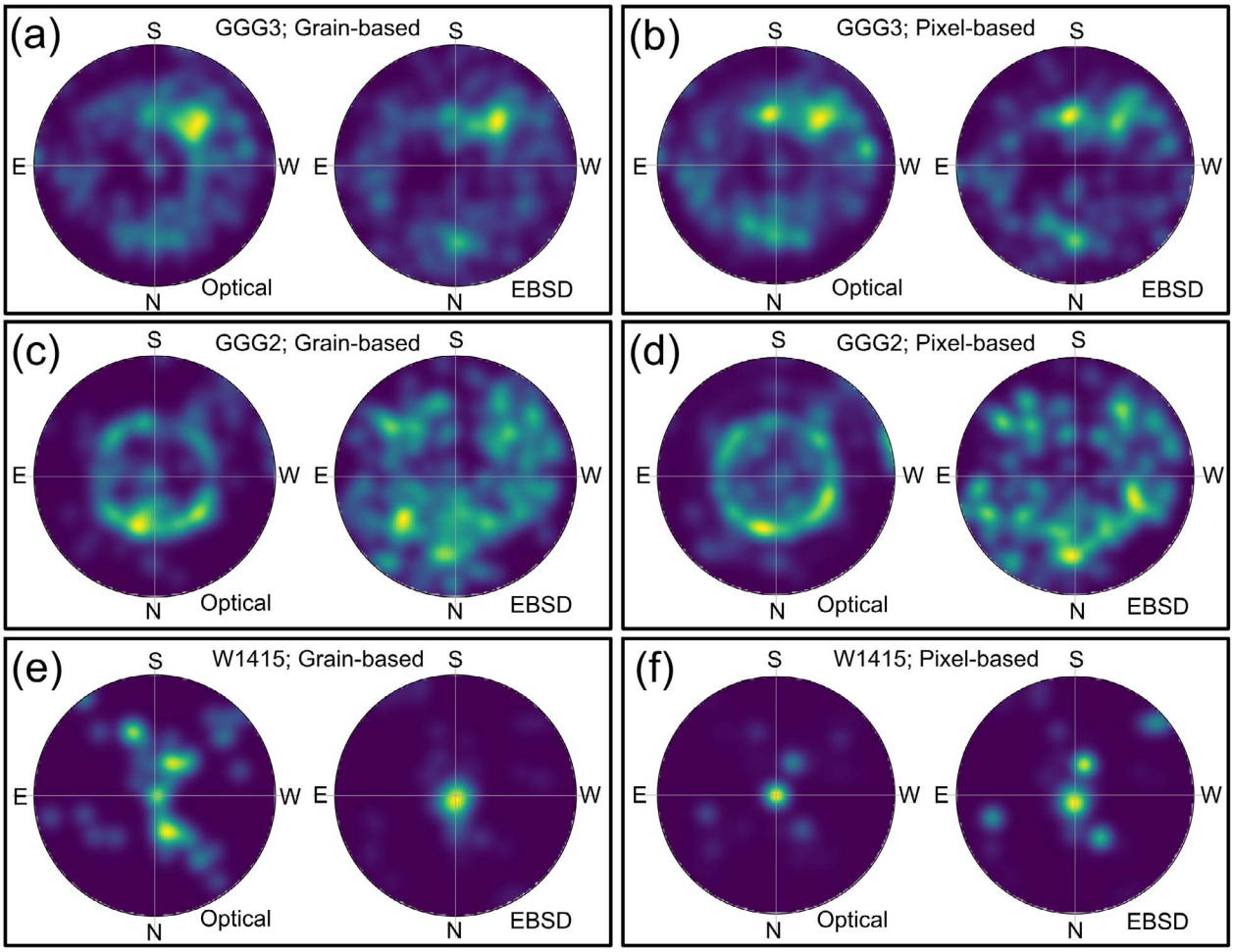


Figure 18 Comparison of optical and EBSD *c*-axis pole figures. (a, c, and e) grain-based pole figures for GGG3, GGG2, and W1415, respectively. (b, d, and f) corresponding pixel-based pole figures constructed from 10 000 randomly sampled pixels. In each panel, the optical result is shown on the left and the EBSD result on the right.

processing of rotation-video data (Furukawa, 2026*b*). Figure 19 shows examples of optical-structure visualization and grain-based and crystallographic analyses.

A simple application is the maximum-intensity image obtained from the rotation sequence. Figure 19a and b compare an XPL image of a microfossil with the corresponding maximum-intensity image. In a single XPL image, parts of the specimen close to extinction become dark and some structures are difficult to recognize. The maximum-intensity image retains the brightest response observed during rotation and therefore reduces this loss of structural information. In Fig. 19b, the fossil outline is more clearly visible. A similar effect can be seen in Fig. 4a and c, where grain-boundary structures are more clearly expressed in the maximum-intensity image.

Extinction-angle maps can also be used independently of the full *c*-axis workflow. Figure 19c and d show maximum-intensity images and extinction-angle maps of garnet from Cazadero. The *c*-axis orientation procedure is restricted to suitable low-retardation uniaxial minerals and is most reliable for relatively thin sections. In contrast, extinction angle can be determined more generally for anisotropic crystals that show measurable extinction during rotation. Extinction-angle maps therefore provide a simple way to visualize spatial variations in optical orientation, including internal features such as undulose extinction and sector zoning.

Figure 19e–l illustrate a connected grain-scale analysis using the YM3 sample. Starting from the maximum-intensity image (Fig. 19e), grains assigned to a selected mineral can be extracted from the classification based on the segmentation used in Fig. 12d. Figure 19f shows grains classified mainly as quartz. Subsequent measurements can then be restricted to quartz rather than applied to all segmented grains.

Examples of outputs produced in NicoNavi are shown in Fig. 19g–l. The *c*-axis maps in Fig. 19g and h encode azimuth over 0–180° together with inclination. Figure 19g shows inclination magnitude over 0–90° before branch determination, whereas Fig. 19h shows inclination over 0–180° after stage-tilt branch determination. Locally mixed colors near $\theta \simeq 90°$ reflect the reduced sensitivity of the stage-tilt method to the inclination branch near 90°. The same grain-scale dataset can also be used to display grain-shape orientations (Fig. 19i), *c*-axis orientation distributions of selected quartz grains (Fig. 19j), grain-size distributions (Fig. 19k), and rose diagrams of grain-shape orientation (Fig. 19l). All of these outputs were generated within NicoNavi, allowing optical images, mineral classification, grain

Downloaded from academic.oup.com/petrology/article/67/11/egag099/9022254 by Hogaku-Bu Library user on 25 November 2026

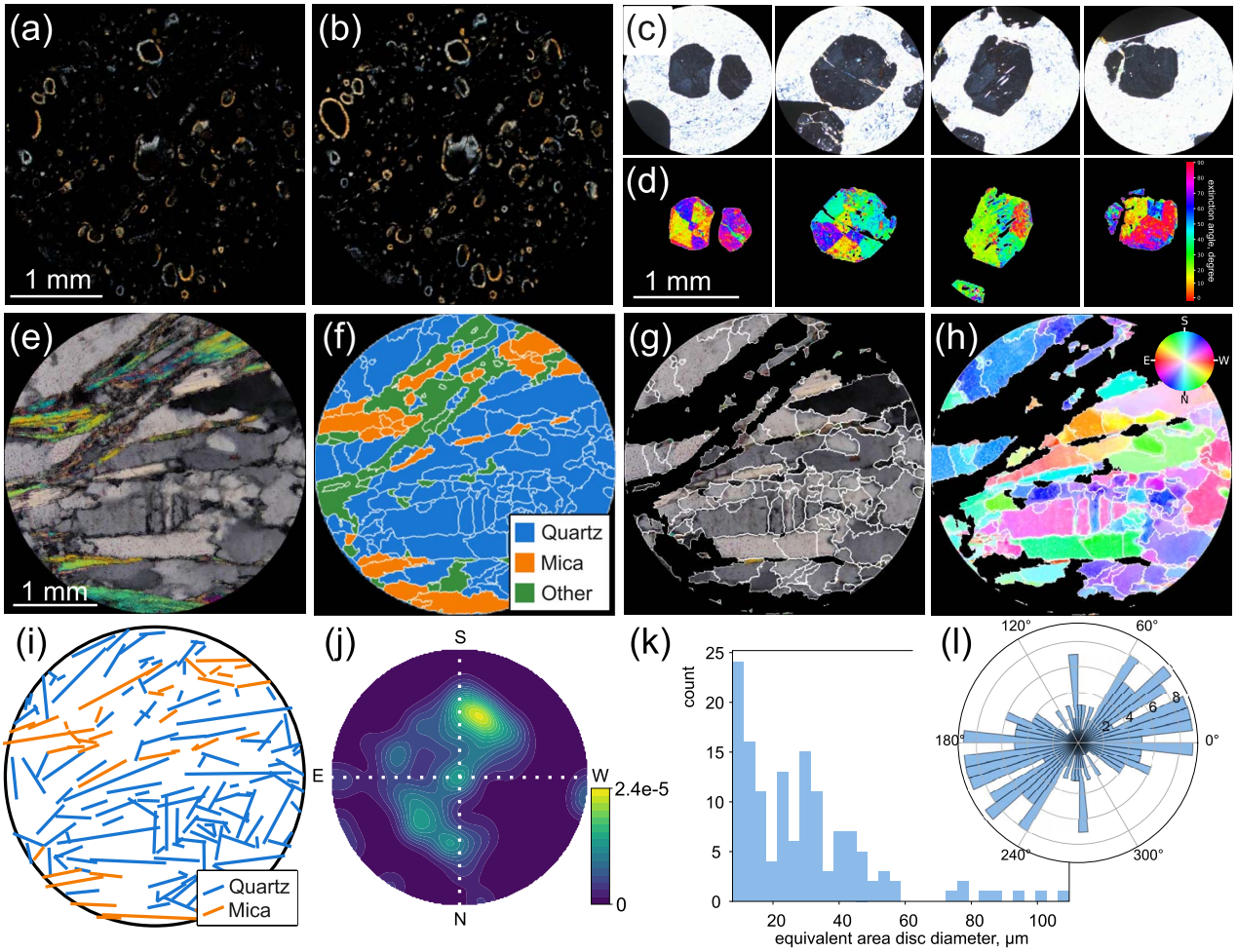


Figure 19 Examples of analyses integrated in NicoNavi. (a) XPL image of a microfossil and (b) corresponding maximum-intensity image. (c) Maximum-intensity images of Cazadero garnet and (d) corresponding extinction-angle maps. (e) Maximum-intensity image of the YM3 sample and (f) phase-selected grain map showing grains classified mainly as quartz. (g) *c*-axis orientation map showing inclination magnitude over 0–90° before inclination-branch determination. (h) Corresponding map showing inclination over 0–180° after inclination-branch determination by stage tilt. (i) Grain-shape orientations shown as the major-axis orientations of equivalent ellipses for grains classified mainly as quartz and mica. (j) *c*-axis orientation distribution of the mainly quartz grains. (k) Grain-size distribution. (l) Rose diagram of grain-shape orientation.

morphology, and crystallographic information to be analyzed within a common workflow.

Conclusions

This study presents a unified optical workflow for quantitative thin-section analysis based on videos acquired with a conventional rotating-stage polarizing microscope. The workflow integrates grain segmentation, semi-supervised mineral classification, grain-size and grain-shape measurements, and three-dimensional *c*-axis orientation analysis within NicoNavi. By using continuous stage rotation rather than stepwise image acquisition, the method simplifies data collection while retaining the optical information required for grain-scale analysis.

Comparison with EBSD shows that the optical results are broadly consistent with crystallographic measurements when thin sections are sufficiently thin and neighboring grains have adequate optical contrast. Under the conditions tested here, thin sections of ~20–35 μm and a 5° segmentation threshold provided the most reliable grain segmentation and grain-based measurements. Segmentation accuracy decreases with increasing section thickness, and boundaries may also be missed where adjacent grains have similar optical responses, particularly for grains with *c*-axes close to the microscope axis. These segmentation errors can propagate into grain counts and shape statistics. The *c*-axis estimates generally reproduce the main orientation distributions observed by EBSD, although errors can arise from limited optical sensitivity to retardation and from incorrect selection of the inclination branch during stage-tilt analysis. Such systematic effects should therefore be considered when interpreting apparent orientation concentrations.

Supplementary Data

Supplementary data are available at *Journal of Petrology* online.

Acknowledgements

The authors thank Jun Muto for providing the EBSD data analyzed for the W1415 sample, Hironobu Harada for insightful discussions and

Downloaded from academic.oup.com/petrology/article/67/11/egag099/9022254 by Hogaku-Bu Library user on 25 November 2026

assistance with thin-section preparation and logistics, Aoka Hoashi for support with EBSD analysis, and Ryo Fukushima for additional insightful discussions. The authors also thank two anonymous reviewers for their constructive comments and suggestions, as well as Pierre Lanari for his thoughtful editorial handling.

Conflict of interest statement

The authors declare no competing interests.

Data availability

The microscopy video dataset supporting this study, together with the EBSD orientation maps used for validation, has been deposited in GFZ Data Services as 'NicoNavi microscope videos and EBSD maps for quantitative thin-section analysis' (Furukawa & Tsujimori, 2025; https://doi.org/10.5880/fidgeo.2025.108). The NicoNavi application is archived in Zenodo (https://doi.org/10.5281/zenodo.23938863) and its source code is available on GitHub (https://github.com/Tan-Furukawa/niconavi_app).

The 3D-printable tilting-stage files are archived in Zenodo (https://doi.org/10.5281/zenodo.22161221) and are also available on GitHub (https://github.com/Tan-Furukawa/niconavi-tilt-stage). Additional methodological details and optical–EBSD comparisons are provided in the Supplementary Material.

References

Acevedo Zamora, M. A., Schrank, C. E. & Kamber, B. S. (2024). Using the traditional microscope for mineral grain orientation determination: a prototype image analysis pipeline for optic-axis mapping (POAM). *Journal of Microscopy* **295**(2), 147–176. https://doi.org/10.1111/jmi.13284.

Achanta, R., Shaji, A., Smith, K., Lucchi, A., Fua, P. & Süsstrunk, S. (2012). SLIC superpixels compared to state-of-the-art superpixel methods. *IEEE Transactions on Pattern Analysis and Machine Intelligence* **34**(11), 2274–2282. https://doi.org/10.1109/TPAMI.2012.120.

de Andrade, V., Vidal, O., Lewin, E., O'Brien, P. J. & Agard, P. (2006). Quantification of electron microprobe compositional maps of rock thin sections: an optimized method and examples. *Journal of Metamorphic Geology* **24**(7), 655–668. https://doi.org/10.1111/j.1525-1314.2006.00660.x.

Bachmann, F., Hielscher, R. & Schaeben, H. (2010). Texture analysis with MTEX—free and open source software toolbox. *Solid State Phenomena* **160**, 63–68. https://doi.org/10.4028/www.scientific.net/SSP.160.63.

Bachmann, F., Hielscher, R. & Schaeben, H. (2011). Grain detection from 2d and 3d EBSD data—specification of the MTEX algorithm. *Ultramicroscopy* **111**(12), 1720–1733. https://doi.org/10.1016/j.ultramic.2011.08.002.

Barraud, J. (2006). The use of watershed segmentation and GIS software for textural analysis of thin sections. *Journal of Volcanology and Geothermal Research* **154**(1–2), 17–33. https://doi.org/10.1016/j.jvolgeores.2005.09.017.

Bradski, G. (2000). The OpenCV library. *Dr. Dobb's Journal of Software Tools* **25**(11), 120–125.

Buchsbaum, G. (1980). A spatial processor model for object colour perception. *Journal of the Franklin Institute* **310**(1), 1–26. https://doi.org/10.1016/0016-0032(80)90058-7.

Carl Zeiss Microscopy GmbH (2024) *The Petrography Analysis Toolbox (PetPAT): Quantitative Analytics for Light Microscopy—ZEISS Axioscan 7 Geo*. Jena, Germany: Carl Zeiss Microscopy GmbH.

Caso, F., Piloni, C. B., Filippi, M., Pezzotta, A., Fazio, E., Visalli, R. *et al.* (2024). Combining traditional and quantitative multiscale structural analysis to reconstruct the tectono-metamorphic evolution of migmatitic basements: the case of the Valpelline Series, Dent-Blanche Tectonic System, Western Alps. *Journal of Structural Geology* **182**, 105099. https://doi.org/10.1016/j.jsg.2024.105099.

Chen, Y., Yi, Y., Dai, Y. & Shi, X. (2024). A multiangle polarised imaging-based method for thin section segmentation. *Journal of Microscopy* **294**(1), 14–25. https://doi.org/10.1111/jmi.13261.

Fisher, N. I. (1993) *Statistical Analysis of Circular Data*. Cambridge: Cambridge University Press.

Friel, J. J. & Lyman, C. E. (2006). Tutorial review: X-ray mapping in electron-beam instruments. *Microscopy and Microanalysis* **12**(1), 2–25. https://doi.org/10.1017/S1431927606060211.

Fueten, F. (1997). A computer-controlled rotating polarizer stage for the petrographic microscope. *Computers & Geosciences* **23**(2), 203–208. https://doi.org/10.1016/S0098-3004(97)85443-X.

Fueten, F. & Goodchild, J. (2001). Quartz c-axes orientation determination using the rotating polarizer microscope. *Journal of Structural Geology* **23**(6-7), 895–902. https://doi.org/10.1016/S0191-8141(00)00161-9.

Furukawa, T. (2026a). Niconavi-tilt-stage: a thin-section holder and tilt stage for NicoNavi. *Zenodo*. https://doi.org/10.5281/zenodo.22161221.

Furukawa, T. (2026b). NicoNavi v0.3.2-beta.2. *Zenodo*. https://doi.org/10.5281/zenodo.23938863.

Furukawa, T. & Tsujimori, T. (2025). NicoNavi microscope videos and EBSD maps for quantitative thin-section analysis. *GFZ Data Services* . https://doi.org/10.5880/fidgeo.2025.108.

Goodchild, J. & Fueten, F. (1998). Edge detection in petrographic images using the rotating polarizer stage. *Computers & Geosciences* **24**(8), 745–751. https://doi.org/10.1016/S0098-3004(98)00054-5.

Heilbronner, R. (2000). Automatic grain boundary detection and grain size analysis using polarization micrographs or orientation images. *Journal of Structural Geology* **22**(7), 969–981. https://doi.org/10.1016/S0191-8141(00)00014-6.

Heilbronner, R. & Barrett, S. (2014) *Image Analysis in Earth Sciences: Microstructures and Textures of Earth Materials*. Berlin, Heidelberg: Springer Berlin Heidelberg.

Heilbronner, R. & Kilian, R. (2017). The grain size(s) of Black Hills Quartzite deformed in the dislocation creep regime. *Solid Earth* **8**(5), 1071–1093. https://doi.org/10.5194/se-8-1071-2017.

Heilbronner, R. & Pauli, C. (1993). Integrated spatial and orientation analysis of quartz c-axes by computer-aided microscopy. *Journal of Structural Geology* **15**(3-5), 369–382. https://doi.org/10.1016/0191-8141(93)90133-U.

Iglesias, J. C. A., Gomes, O.d. F. M. & Paciornik, S. (2011). Automatic recognition of hematite grains under polarized reflected light microscopy through image analysis. *Minerals Engineering* **24**(12), 1264–1270. https://doi.org/10.1016/j.mineng.2011.04.015.

Jiang, F., Gu, Q., Hao, H., Li, N., Wang, B. & Hu, X. (2018). A method for automatic grain segmentation of multi-angle cross-polarized microscopic images of sandstone. *Computers & Geosciences* **115**, 143–153. https://doi.org/10.1016/j.cageo.2018.03.010.

Lanari, P., Vho, A., Bovay, T., Airaghi, L. & Centrella, S. (2019). Quantitative compositional mapping of mineral phases by electron probe microanalyser. *Geological Society, London, Special Publications* **478**, 39–63. https://doi.org/10.1144/SP478.4.

Downloaded from academic.oup.com/petrology/article/67/11/egag099/9022254 by Hogaku-Bu Library user on 25 November 2026

Launeau, P., Cruden, A. R. & Bouchez, J. L. (1994). Mineral recognition in digital images of rocks: a new approach using multichannel classification. *The Canadian Mineralogist* **32**(4), 919–933.

Li, Y., Onasch, C. M. & Guo, Y. (2008). GIS-based detection of grain boundaries. *Journal of Structural Geology* **30**(4), 431–443. https://doi.org/10.1016/j.jsg.2007.12.007.

Medalia, A. I. (1971). Dynamic shape factors of particles. *Powder Technology* **4**(3), 117–138. https://doi.org/10.1016/0032-5910(71)80021-9.

Muto, J., Hirth, G., Heilbronner, R. & Tullis, J. (2011). Plastic anisotropy and fabric evolution in sheared and recrystallized quartz single crystals. *Journal of Geophysical Research: Solid Earth* **116**(B2), B02206. https://doi.org/10.1029/2010JB007891.

Ni, J., Singh, M. K. & Bahlmann, C. (2012) Fast radial symmetry detection under affine transformations. In: *2012 IEEE Conference on Computer Vision and Pattern Recognition*. Piscataway, NJ, USA: IEEE, pp. 932–939. https://doi.org/10.1109/CVPR.2012.6247768.

Ortolano, G., Visalli, R., Godard, G. & Cirrincione, R. (2018). Quantitative X-ray map analyser (Q-XRMA): a new GIS-based statistical approach to mineral image analysis. *Computers & Geosciences* **115**, 56–65. https://doi.org/10.1016/j.cageo.2018.03.001.

Ortolano, G., Fazio, E., Visalli, R., Alsop, G. I., Pagano, M. & Cirrincione, R. (2020). Quantitative microstructural analysis of mylonites formed during Alpine tectonics in the Western Mediterranean Realm. *Journal of Structural Geology* **131**, 103956. https://doi.org/10.1016/j.jsg.2019.103956.

Pirard, E. (2004) Image measurements. In: Francus P. (ed) *Image Analysis, Sediments and Paleoenvironments*, Vol. **7**. Dordrecht: Springer, pp. 59–86.

Prior, D. J., Boyle, A. P., Brenker, F., Cheadle, M. C., Day, A., Lopez, G., Peruzzi, L., Potts, G., Reddy, S., Spiess, R., Timms, N. E., Trimby, P., Wheeler, J. & Zetterstrom, L. (1999). The application of electron backscatter diffraction and orientation contrast imaging in the SEM to textural problems in rocks. *American Mineralogist* **84**(11–12), 1741–1759. https://doi.org/10.2138/am-1999-11-1204.

Reddy, B. S. & Chatterji, B. N. (1996). An FFT-based technique for translation, rotation, and scale-invariant image registration. *IEEE Transactions on Image Processing* **5**(8), 1266–1271. https://doi.org/10.1109/83.506761.

Roda, M., Zucali, M., Corti, L., Visalli, R., Ortolano, G. & Spalla, M. I. (2021). Blueschist mylonitic zones accommodating syn-subduction exhumation of deeply buried continental crust: the example of the Rocca Canavese thrust sheets unit (Sesia–Lanzo Zone, Italian Western Alps). *Swiss Journal of Geosciences* **114**, 6. https://doi.org/10.1186/s00015-021-00385-7.

Roy Choudhury, K., Meere, P. A. & Mulchrone, K. F. (2006). Automated grain boundary detection by CASRG. *Journal of Structural Geology* **28**(3), 363–375. https://doi.org/10.1016/j.jsg.2005.12.010.

Stöckhert, B. & Duyster, J. (1999). Discontinuous grain growth in recrystallised vein quartz—implications for grain boundary structure, grain boundary mobility, crystallographic preferred orientation, and stress history. *Journal of Structural Geology* **21**(10), 1477–1490. https://doi.org/10.1016/S0191-8141(99)00084-X.

Tarquini, S. & Favalli, M. (2010). A Microscopic Information System (MIS) for petrographic analysis. *Computers & Geosciences* **36**(5), 665–674. https://doi.org/10.1016/j.cageo.2009.09.017.

Thompson, S., Fueten, F. & Bockus, D. (2001). Mineral identification using artificial neural networks and the rotating polarizer stage. *Computers & Geosciences* **27**(9), 1081–1089. https://doi.org/10.1016/S0098-3004(00)00153-9.

Visalli, R., Ortolano, G., Godard, G. & Cirrincione, R. (2021). Micro-Fabric Analyzer (MFA): a new semiautomated ArcGIS-based edge detector for quantitative microstructural analysis of rock thin-sections. *ISPRS International Journal of Geo-Information* **10**(2), 51. https://doi.org/10.3390/ijgi10020051.

Winiarski, B., Gholinia, A., Mingard, K., Gee, M., Thompson, G. & Withers, P. J. (2021). Correction of artefacts associated with large area EBSD. *Ultramicroscopy* **226**, 113315. https://doi.org/10.1016/j.ultramic.2021.113315.

Xypolias, P. (2010). Vorticity analysis in shear zones: a review of methods and applications. *Journal of Structural Geology* **32**(12), 2072–2092. https://doi.org/10.1016/j.jsg.2010.08.009.

Zheng, D., Hou, L., Hu, X., Hou, M., Dong, K., Hu, S., Teng, R. & Ma, C. (2024). Sediment grain segmentation in thin-section images using dual-modal vision transformer. *Computers & Geosciences* **191**, 105664. https://doi.org/10.1016/j.cageo.2024.105664.

Zhou, Y., Starkey, J. & Mansinha, L. (2004). Segmentation of petrographic images by integrating edge detection and region growing. *Computers & Geosciences* **30**(8), 817–831. https://doi.org/10.1016/j.cageo.2004.05.002.

Zhu, X. & Ghahramani, Z. (2002) *Learning from Labeled and Unlabeled Data with Label Propagation (Technical Report)*. Pittsburgh, PA: School of Computer Science, Carnegie Mellon University, (Technical Report CMU-CALD-02-107, School of Computer Science, Carnegie Mellon University).

Downloaded from academic.oup.com/petrology/article/67/11/egag099/9022254 by Hogaku-Bu Library user on 25 November 2026

© The Author(s) 2026. Published by Oxford University Press. This is an Open Access article distributed under the terms of the Creative Commons Attribution License (https://creativecommons.org/licenses/by/4.0/), which permits unrestricted reuse, distribution, and reproduction in any medium, provided the original work is properly cited.
Journal of Petrology, 2026, 67(11),
https://doi.org/10.1093/petrology/egag099
Original Manuscript

Supplementary Material

Quantitative Petrography from Thin-Section Videos: A Unified Optical Workflow for Grain-Scale Microstructure Analysis

Tan Furukawa Tatsuki Tsujimori

Contents

S1 Details of image processing and modeling **2**
S1.1 Stage rotation-center detection using the fast radial symmetry transform 2
S1.2 Stage rotation-center refinement using four-fold symmetry 2
S1.3 HSV angle-map cleaning 3
S1.4 SLICO segmentation parameters 3
S1.5 Interference-color model 5
S1.6 Interference-color fitting 5
S1.7 Focus stacking of tilted images 6
S1.8 Robust color calibration for stage-tilt prediction 6
S1.9 Semi-supervised phase classification 7

S2 Additional optical–EBSD comparisons **9**
S2.1 Per-sample azimuth and inclination comparisons 9
S2.2 Grain-based c-axis orientation distributions 10
S2.3 Pixel-based c-axis orientation distributions 11
S2.4 Grain-shape orientation distributions 12

S1 Details of image processing and modeling

S1.1 Stage rotation-center detection using the fast radial symmetry transform

We begin with the cross-polarized light (XPL) rotation video and stack the pre-processed frames I_i^{XPL}. The pixelwise maximum is

$$I_{\mathrm{stacked}}^{\mathrm{XPL}}(x, y) = \max_i I_i^{\mathrm{XPL}}(x, y), \tag{S1}$$

for pixel coordinates (x, y).

The maximum-intensity image (Fig. S1a) was smoothed (Gaussian, 11×11, $\sigma = 5$) and downsampled to a width of 400 px. Taking the image centroid as a provisional origin, a search radius r was set to 0.7 times the distance from the centroid to the nearest image border. The fast radial symmetry transform (FRST) was then evaluated at radii of 10, 50, 75, 100, 150, 200, and 250 px, and the resulting vote map was blurred (Gaussian, 101×101, $\sigma = 21$). The global maximum of this map provides an initial estimate of the rotation center, denoted $c_0 = (x_0, y_0)$ (Fig. S1b).

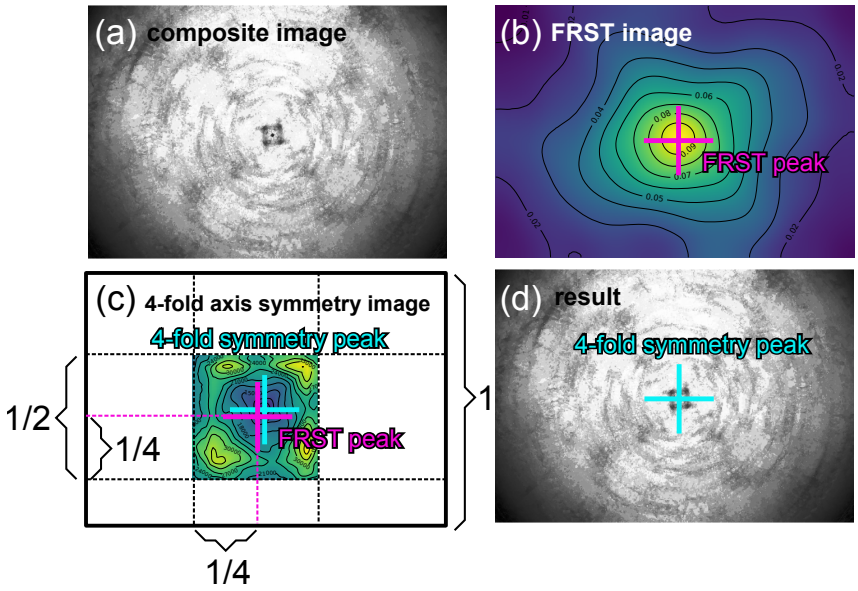


Figure S1: Rotation-center detection workflow. (a) Pixelwise maximum-intensity image $I_{\mathrm{stacked}}^{\mathrm{XPL}}$ computed from the discretized rotation video (Eq. (S1)). (b) Fast radial symmetry transform score map $FRST(x, y)$ whose maximum provides the initial center estimate c_0. (c) Local four-fold symmetry score ($\Sigma(x, y)$; Eq. (S2)) used to refine the center. (d) Composite view showing the maximum-intensity image with the final center overlaid.

S1.2 Stage rotation-center refinement using four-fold symmetry

We refine the FRST result by exploiting the approximate four-fold symmetry of the maximum-intensity image. Under XPL, minerals exhibit similar brightness patterns every 90° of stage rotation, so the maximum-intensity image is closest to four-fold symmetric about the true rotation center (Fig. S1c). Within a square window around c_0, we consider each candidate pixel (x, y), extract the largest square patch $P_{x,y}$ centered at (x, y) that fits inside the image, and compute

$$\Sigma(x, y) = \frac{1}{|P_{x,y}|} \sum_{q=0}^{3} \left| P_{x,y}^{(q)} - P_{x,y}^{((q+1) \bmod 4)} \right|^2, \tag{S2}$$

where $|P_{x,y}|$ is the number of pixels in the patch and $P^{(q)}_{x,y}$ is the patch rotated by $90° \times q$ about (x, y). The score $\Sigma(x, y)$ approaches zero at a perfectly four-fold symmetric point (Fig. S1c). We adopt the minimizer of $\Sigma(x, y)$ within the search window as the final stage-rotation center (Fig. S1d).

S1.3 HSV angle-map cleaning

We introduce a new parameter that represents the darkness, simply defined as

$$K_i = 1 - V_i. \tag{S3}$$

Hue differences between neighboring pixels are evaluated using the circular distance, because $H = 1$ and $H = 0$ should evaluate as the same hue,

$$\Delta H_{ij} = \min(|H_i - H_j|,\, 1 - |H_i - H_j|)\,, \tag{S4}$$

where H_i and V_i are the hue and value of pixel i defined in Eq. (4) of the main text.

The HSV angle map is cleaned by iterative propagation from neighboring pixels. For each pixel i, a color candidate must have a similar hue and a sufficiently larger value, whereas a dark candidate is defined by a low value:

$$\begin{aligned} \mathcal{C}_i &= \{j \in \mathcal{N}(i) \mid V_j \geq V_i + \delta_V,\ \Delta H_{ij} \leq \delta_H\}\,, \\ \mathcal{B}_i &= \{j \in \mathcal{N}(i) \mid V_j \leq V_{\text{source}}\}\,, \end{aligned} \tag{S5}$$

where $\mathcal{N}(i)$ denotes the neighboring pixels. Thus, $\mathcal{C}_i$ propagates similar orientation colors within grains, whereas $\mathcal{B}_i$ preserves and propagates dark features associated with grain boundaries and other low-intensity structures.

For pixels with $V_i > V_{\text{blur}}$, only color candidates are considered, and the candidate with the largest V_j is selected. For pixels with $V_i \leq V_{\text{blur}}$, both color and dark candidates are considered; color candidates are weighted by V_j, whereas dark candidates are weighted by $K_j = 1 - V_j$. The highest-weight candidate is denoted j^*. The pixel color $\mathbf{C}_i$ is then updated as

$$\mathbf{C}_i^{(n+1)} = \begin{cases} \mathbf{C}_i^{(n)}, & V_i \leq V_{\text{keep}} \text{ or } j^* \text{ is undefined}, \\ (1-a)\mathbf{C}_i^{(n)} + a\mathbf{C}_{j^*}^{(n)}, & \text{otherwise}. \end{cases} \tag{S6}$$

Pixels darker than V_{keep} are therefore retained, while brighter pixels are progressively replaced by nearby colors of similar hue. Pixels with low V can instead be influenced by dark neighbors, preventing dark boundary features from being filled during propagation. Repeated application of Eq. (S6) suppresses small-scale color variations within grains while retaining major hue discontinuities and dark boundaries.

The thresholds originally defined from image lightness were converted to the corresponding values of V through their common relation to the inclination proxy. We used $V_{\text{keep}} = 39/255$, $V_{\text{source}} = 62/255$, $V_{\text{blur}} = 60/255$, $\delta_V = 5/255$, and $\delta_H = 10°/90°$, with $a = 0.5$. Propagation was terminated before full convergence to prevent long-range color spreading between grains with gradually varying optical orientations.

S1.4 SLICO segmentation parameters

The cleaned HSV angle map was initially oversegmented using the SLICO variant of the simple linear iterative clustering (SLIC) superpixel algorithm. SLICO groups neighboring pixels according to both color similarity and spatial proximity, producing compact regions that serve as the initial units for subsequent orientation-based merging. We used a region size of 30 pixels, a ruler value of 20.0, 10 iterations, and a minimum element size of 25% of the average superpixel size

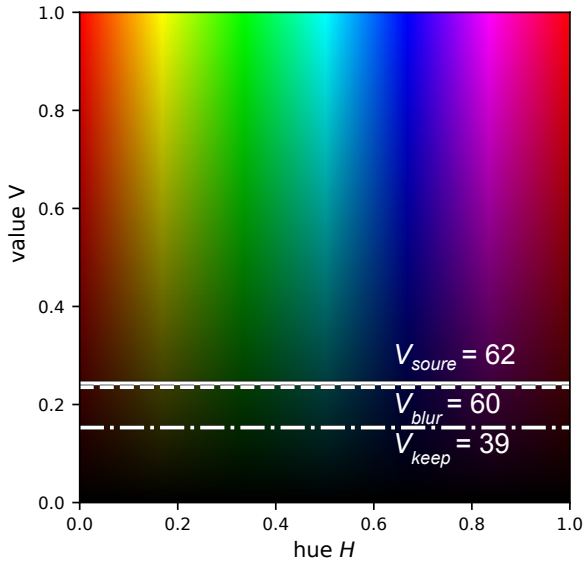


Figure S2: H-V color space and the threshold parameters used to classify high and low values of V, given here on the 0–255 scale: $V_{\mathrm{source}} = 62$, $V_{\mathrm{blur}} = 60$, and $V_{\mathrm{keep}} = 39$.

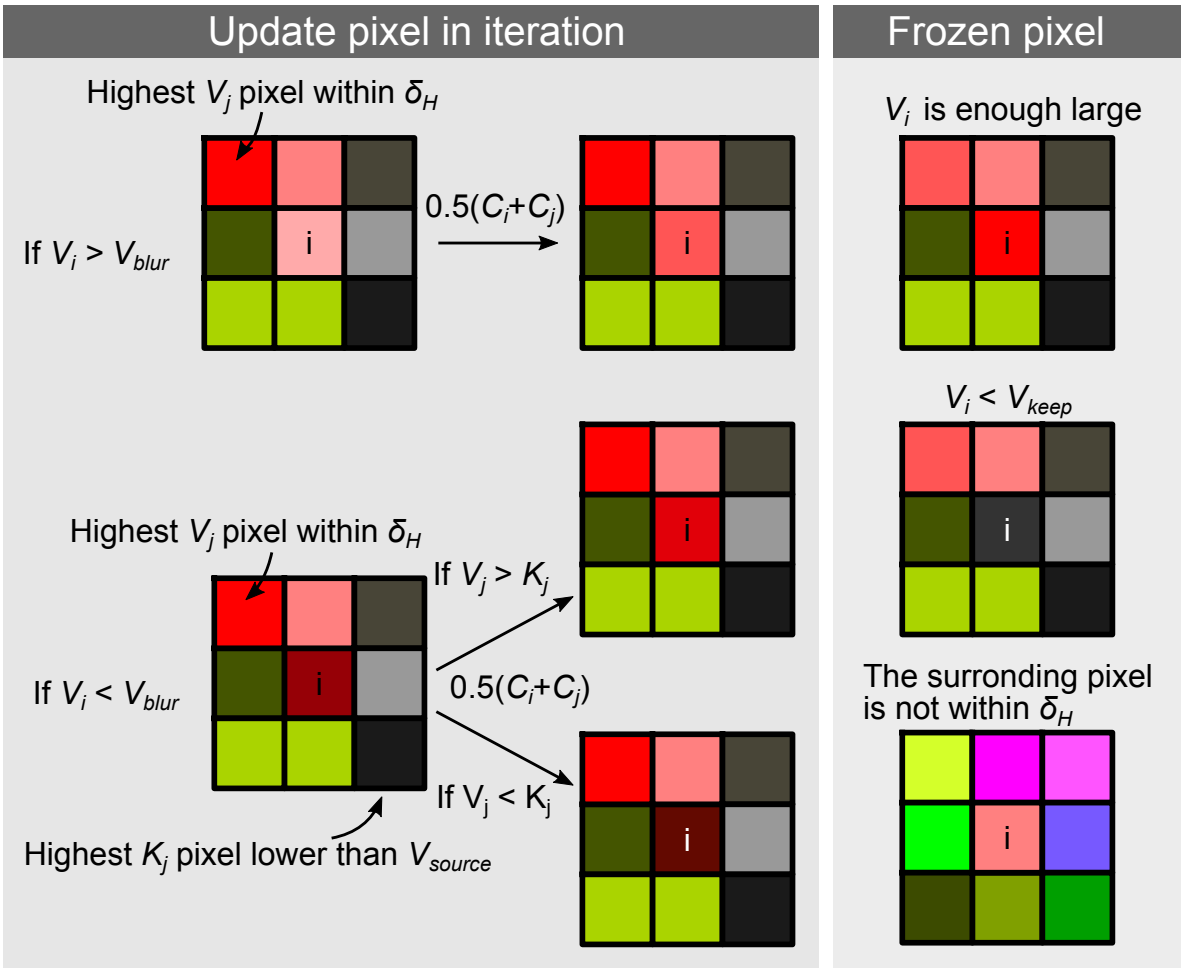


Figure S3: Schematic diagram of grain color update by each iteration.

S1.5 Interference-color model

The theoretical interference colors used in this study are calculated using Jones calculus (Jones, 1941). A retarder with retardation Γ and a rotation by angle χ are represented as

$$\mathsf{J}(\Gamma,\lambda)=\begin{pmatrix} e^{\mathrm{i}2\pi\Gamma/\lambda} & 0\\ 0 & 1\end{pmatrix},\qquad \mathsf{Rot}(\chi)=\begin{pmatrix}\cos\chi & -\sin\chi\\ \sin\chi & \cos\chi\end{pmatrix}, \tag{S7}$$

where i is the imaginary unit and λ is the wavelength. A retarder whose slow axis is oriented at χ is therefore represented by $\mathsf{Rot}(-\chi)\mathsf{J}(\Gamma,\lambda)\mathsf{Rot}(\chi)$.

For a mineral with retardation $R(\theta,t)$ and slow-axis azimuth φ, followed by a λ-plate with retardation R_0 and slow-axis azimuth χ_0, the electric field after the analyzer is

$$\mathbf{E}(\lambda)=\mathsf{P}_y\mathsf{Rot}(-\chi_0)\mathsf{J}(R_0,\lambda)\mathsf{Rot}(\chi_0)\mathsf{Rot}(-\varphi)\mathsf{J}(R(\theta,t),\lambda)\,\mathsf{Rot}(\varphi)\mathbf{e}_x, \tag{S8}$$

where $\mathbf{e}_x$ is the linearly polarized light transmitted by the polarizer and P_y represents the analyzer. The transmitted spectral intensity is then

$$I(\lambda)=\|\mathbf{E}(\lambda)\|_2^2\,. \tag{S9}$$

The spectrum $I(\lambda)$ is calculated over the visible wavelength range, weighted by the spectral distribution of the illuminant and the CIE color-matching functions, and converted from the resulting tristimulus values to sRGB. The brightness factor α used in Azimuth of the main text uniformly scales the modeled vector to account for differences in illumination intensity and camera response.

The modeled additive color $\mathbf{c}(\theta)$ used in Eq. (10) of the main text is calculated with the λ-plate included and the mineral slow axis aligned with that of the plate.

S1.6 Interference-color fitting

The angle θ is determined by fitting an observed color to the theoretical color series described in Section S1.5. The procedure is described below for the grain-wise inclination fit of Inclination magnitude of the main text; the same scheme is applied pixel by pixel to the two λ-plate images in Azimuth of the main text. The theoretical colors are calculated for discrete inclination values θ_k and written as $\mathbf{c}_k=\mathbf{c}(\theta_k)$. For each grain g, the observed color $\mathbf{y}_g$ is modeled as

$$\mathbf{y}_g\approx\alpha_{\mathrm{add}}\mathbf{c}_{k_g},\qquad k_g=\arg\min_k\|\mathbf{y}_g-\alpha_{\mathrm{add}}\mathbf{c}_k\|_2^2\,, \tag{S10}$$

where $\alpha_{\mathrm{add}}\in[0,1]$ is a brightness factor common to all grains and k_g specifies the inclination assigned to grain g. Only this scalar brightness correction is fitted; no color matrix or channel-dependent offset is introduced, to avoid degeneracy between color correction and inclination.

An initial value of α_{add} is obtained by grid search. For each candidate α, the closest theoretical color is assigned independently to every grain, and the value giving the smallest mean RGB residual is selected:

$$\alpha_0=\arg\min_\alpha\frac{1}{G}\sum_g\min_k\|\mathbf{y}_g-\alpha\mathbf{c}_k\|_2\,, \tag{S11}$$

where G is the number of grains.

Starting from α_0, α_{add} and the inclination assignments are refined by minimizing

$$\mathcal{L}_{\mathrm{fit}}=\frac{1}{3G}\sum_{g,c}\rho_\delta\big(y_{gc}-\alpha_{\mathrm{add}}c_{k_g,c}\big)\,, \tag{S12}$$

where c indexes the RGB channels and ρ_δ is the Huber loss (Huber, 1964). The objective was minimized by alternating Huber iteratively reweighted least squares (IRLS) for α_{add} with

reassignment of k_g using Eq. (S10). The two steps were repeated until the brightness factor and all inclination assignments converged, with a maximum of 30 iterations.

This robust alternating optimization limits the influence of grains whose colors are poorly represented by the theoretical series, for example because of boundary mixing, image artifacts, or phases other than the target mineral.

S1.7 Focus stacking of tilted images

Let $\mathbf{I}_f(x, y)$ denote the RGB value at pixel (x, y) in frame f of a focus-sweep video, and let $G_f(x, y)$ be its grayscale value. A local sharpness score was calculated as the absolute discrete Laplacian, and the frame with the largest score was selected at each pixel. To suppress isolated changes in the selected frame within low-texture regions, only the resulting frame-index map was smoothed with a 5×5 median filter. The stacked image was then assembled as

$$\begin{aligned} S_f(x, y) &= \left|\nabla^2 G_f(x, y)\right|, \\ \widetilde{k}(x, y) &= \arg\max_f S_f(x, y), \\ k(x, y) &= \operatorname*{median}_{(u,v)\in\mathcal{N}_5(x,y)} \widetilde{k}(u, v), \\ \mathbf{I}_{\text{stack}}(x, y) &= \mathbf{I}_{k(x,y)}(x, y), \end{aligned}$$

where $\mathcal{N}_5(x, y)$ is the 5×5 neighborhood centered on (x, y). Because the median filter is applied to the frame indices rather than to the RGB channels, every output pixel retains a measured color from one input frame.

S1.8 Robust color calibration for stage-tilt prediction

The theoretical colors used to predict the response to stage tilting were calibrated against the measured colors in the untilted image. For each grain g, one representative pixel was selected as the valid pixel nearest to the grain centroid. Valid pixels were required to lie within the grain, the circular field of view, and the region shared by the registered untilted and tilted images, and to have finite azimuth, inclination, and RGB values. Grains containing fewer than five valid pixels were excluded. Using one pixel per grain reduces contamination from grain boundaries and prevents large grains from dominating the fit.

The measured RGB color at the representative pixel is denoted by $\mathbf{y}_g$, and the corresponding theoretical color calculated from the Jones model is denoted by $\mathbf{c}_g = \mathbf{c}(\varphi_g, \theta_g)$. Here, φ_g and θ_g are the azimuth and corrected inclination of grain g, respectively. The measured and theoretical colors are related by

$$\mathbf{y}_g \approx \alpha_{\text{color}} M \mathbf{c}_g + \mathbf{b}, \qquad \operatorname{tr}(M) = 3, \tag{S13}$$

where $\alpha_{\text{color}} \in [0, 1]$ is a common brightness factor, M is a 3×3 color-correction matrix, and $\mathbf{b}$ is an RGB offset. The trace constraint removes the scale degeneracy between α_{color} and M. The RGB values are scaled to 0–1 during fitting, and the parameters are obtained by minimizing

$$\mathcal{L} = \frac{1}{3G} \sum_{g,c} \rho_\delta(r_{gc}) + 10\,\overline{(M - I)^2} + 2\,\overline{\mathbf{b}^2}, \qquad r_{gc} = y_{gc} - \left(\alpha_{\text{color}} M \mathbf{c}_g + \mathbf{b}\right)_c, \tag{S14}$$

where G is the number of fitted grains, c indexes the RGB channels, I is the identity matrix, and ρ_δ is the Huber loss (Huber, 1964). The two regularization terms constrain M toward I and $\mathbf{b}$ toward zero, limiting overfitting when the sampled colors occupy only part of the RGB color space.

The objective in Eq. (S14) was minimized using Huber IRLS. The fit was initialized with $M = I$ and $\mathbf{b} = 0$, after which $(M, \mathbf{b})$ and α_{color} were estimated alternately because the product $\alpha_{\text{color}} M$ is bilinear. The resulting transformation was applied identically to the colors predicted for the two inclination branches, so that both hypotheses were compared in the measured-image color space.

S1.9 Semi-supervised phase classification

The classification is performed on individual grains defined by the grain segmentation. For each grain g, seven features are calculated from grain shape, size, color in the maximum-retardation color map, and spatial position. Shape is represented by the logarithmic elongation

$$E_g = \log\left[\left(\frac{\lambda_{2,g} + 1/12}{\lambda_{1,g} + 1/12}\right)^{1/2}\right], \qquad \lambda_{1,g} \le \lambda_{2,g}, \tag{S15}$$

where $\lambda_{1,g}$ and $\lambda_{2,g}$ are the eigenvalues of the covariance matrix of the pixel coordinates within the grain. The added variance of $1/12$, corresponding to a unit-square pixel, keeps the measure finite for grains only one pixel wide. Grain size is represented by $\log A_g$, where A_g is the grain area in pixels.

The three color features are the within-grain median CIELAB components,

$$\widetilde{L^*}_g, \qquad \widetilde{a^*}_g, \qquad \widetilde{b^*}_g. \tag{S16}$$

Median values are used to reduce the influence of local color variations, inclusions, and pixels near grain boundaries. The two spatial features are the normalized grain-centroid coordinates,

$$\bar{x}_g = \frac{x_g}{W - 1}, \qquad \bar{y}_g = \frac{y_g}{H - 1}, \tag{S17}$$

where W and H are the image width and height in pixels, respectively.

The feature vector used for the calculations in this paper is therefore

$$\mathbf{x}_g = \left(E_g,\, \log A_g,\, \frac{\widetilde{L^*}_g}{50},\, \frac{\widetilde{a^*}_g}{50},\, \frac{\widetilde{b^*}_g}{50}\right), \tag{S18}$$

and the N segmented grains form a feature matrix

$$\mathbf{X} \in \mathbb{R}^{N \times 5}. \tag{S19}$$

Dividing the CIELAB components by 50 reduces the contribution of their larger numerical ranges and prevents the color features from overwhelming the logarithmic elongation and area in the Euclidean-distance calculation. Because the same divisor is applied to all three components, their relative distances in CIELAB space are retained. Shape, size, and color were used for the calculations presented in this paper, whereas position was not used. NicoNavi permits the normalized centroid coordinates to be included as optional features; when selected, $0.2\bar{x}_g$ and $0.2\bar{y}_g$ are appended to $\mathbf{x}_g$.

The user assigns class labels to a subset of grains. For each class c, the score of grain g is determined from the nearest manually labeled grain belonging to that class,

$$s_{gc} = \max_{g' \in \mathcal{L}_c} \exp\left(-\frac{\left\|\mathbf{x}_g - \mathbf{x}_{g'}\right\|_2^2}{2\sigma^2}\right), \tag{S20}$$

where $\mathcal{L}_c$ is the set of manually labeled grains in class c. The bandwidth σ is the median of the nonzero distances from each grain to its nearest manually labeled grain. The scores are normalized over the classes to give

$$p_{gc} = \frac{s_{gc}}{\sum_{c'} s_{gc'}}. \tag{S21}$$

Thus, p_{gc} is based solely on similarity to the manually labeled prototypes; no graph-based `LabelPropagation` term is included. The predicted mineral class is the class with the largest probability,

$$\hat{c}_g = \arg\max_c p_{gc}. \tag{S22}$$

After at least one manual label has been assigned, every segmented grain is assigned to one of the user-defined classes. Manually assigned labels are always retained and are not replaced by automatic predictions. The probabilities and classifications are recalculated whenever the user adds or removes a manual label.

S2 Additional optical–EBSD comparisons

S2.1 Per-sample azimuth and inclination comparisons

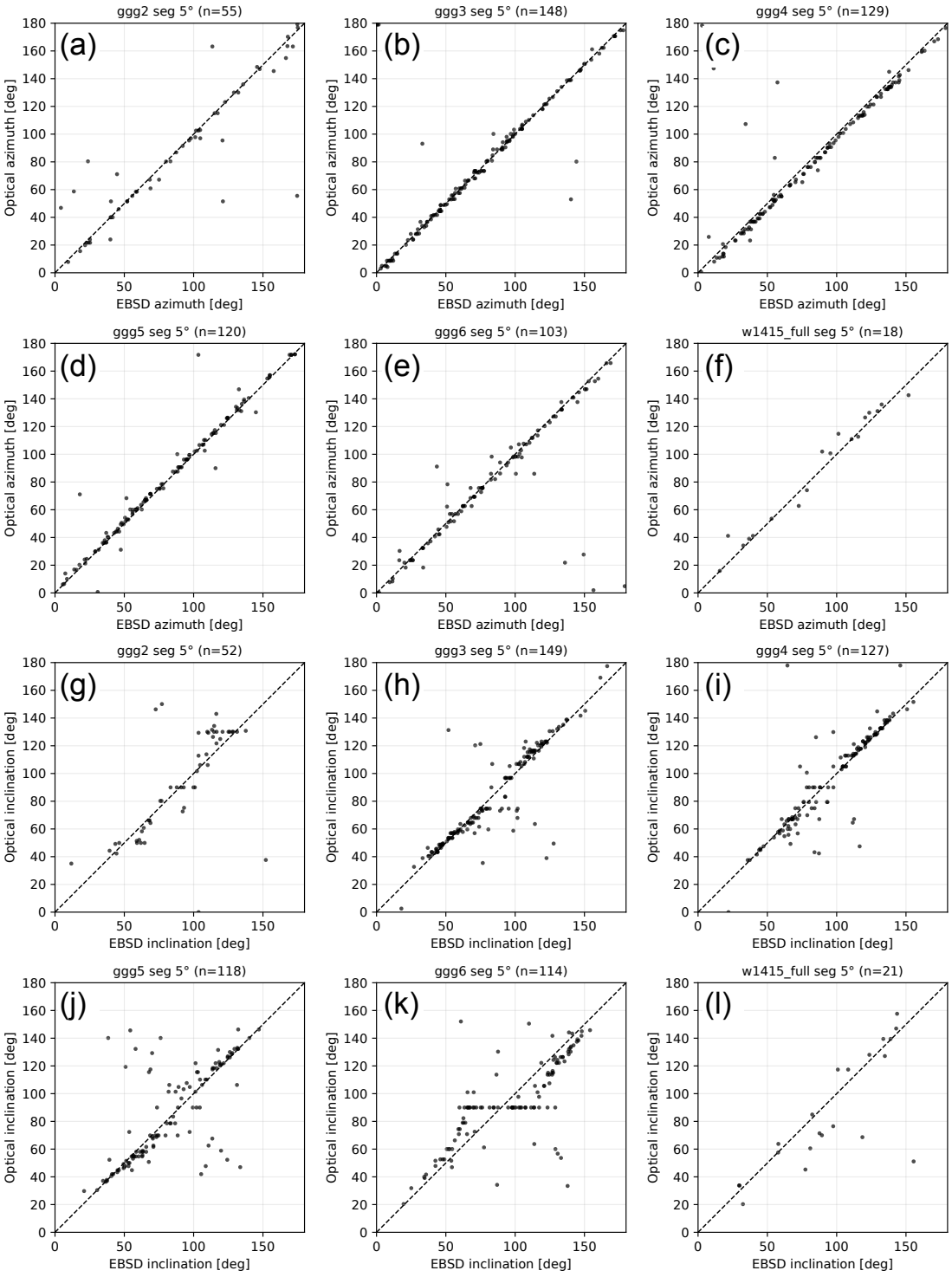


Figure S4: Azimuth and inclination comparisons between optical and EBSD measurements for all samples using a 5° segmentation threshold. Panels (a–f) show azimuth and panels (g–l) show inclination. Dashed lines show the 1:1 relation.

S2.2 Grain-based c-axis orientation distributions

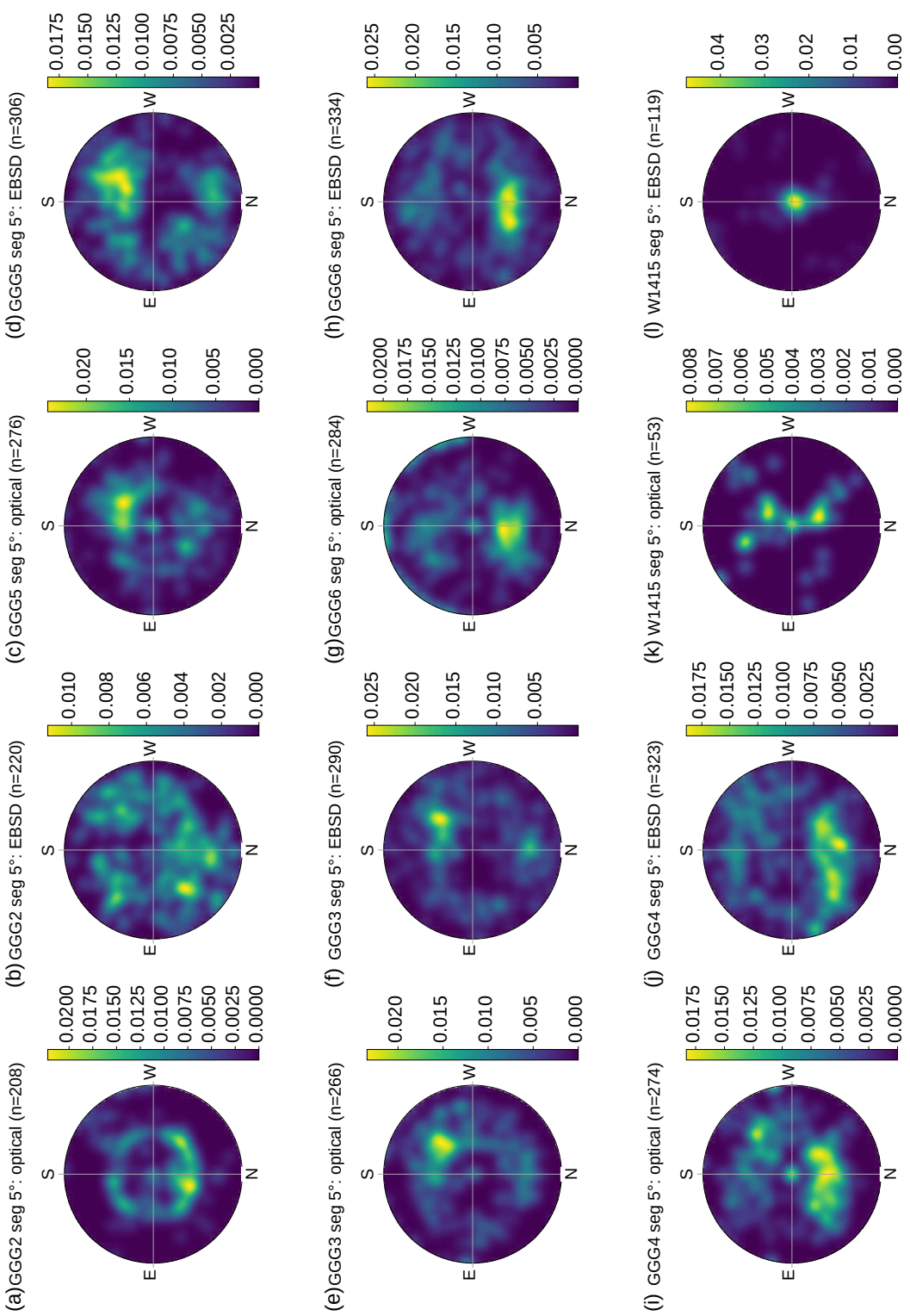


Figure S5: Grain-based c-axis orientation-density plots derived from optical and EBSD measurements for all samples using a 5° segmentation threshold.

S2.3 Pixel-based c-axis orientation distributions

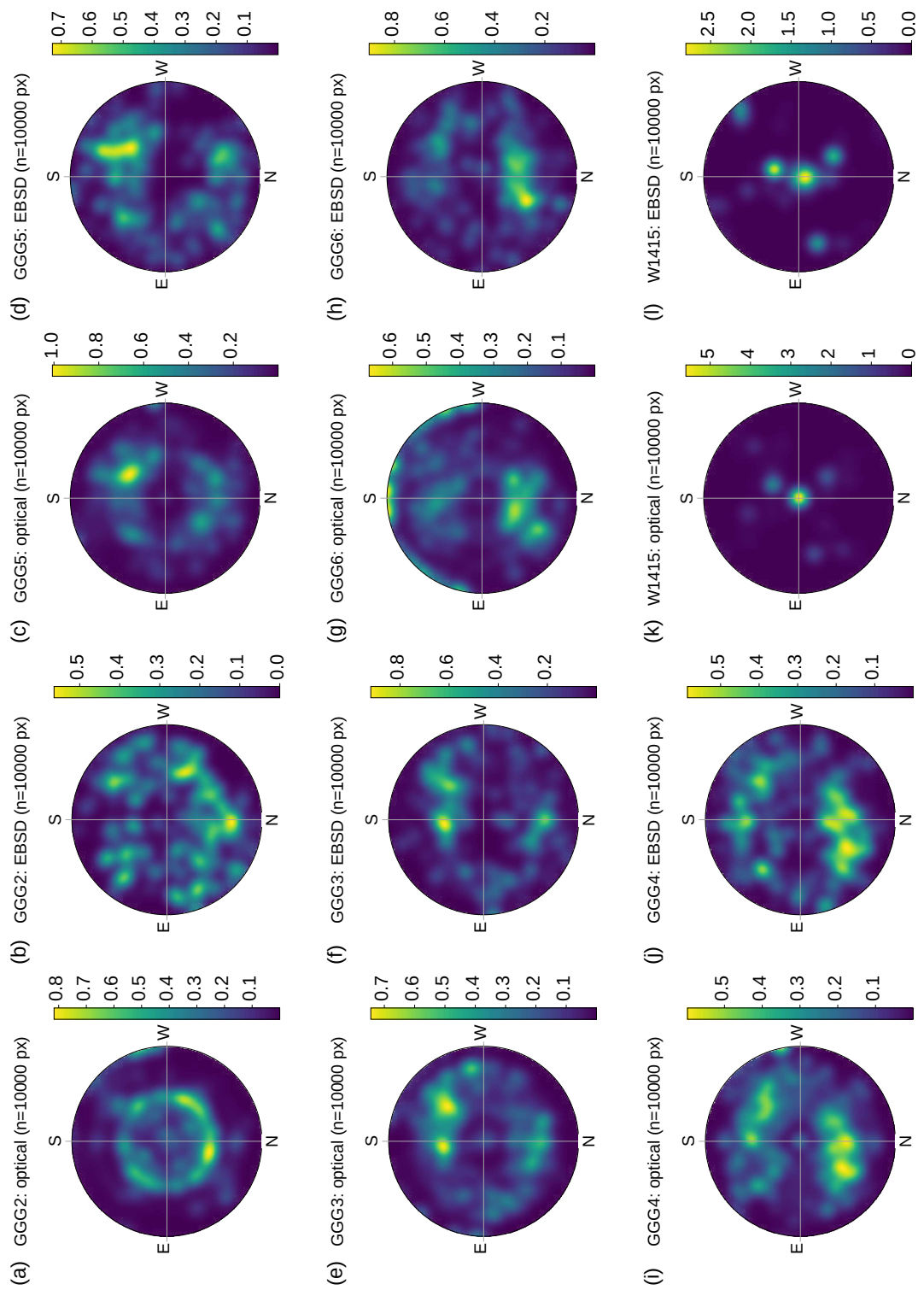


Figure S6: Pixel-based c-axis orientation-density plots derived from optical and EBSD measurements for all samples. Each distribution contains 10,000 sampled pixels.

S2.4 Grain-shape orientation distributions

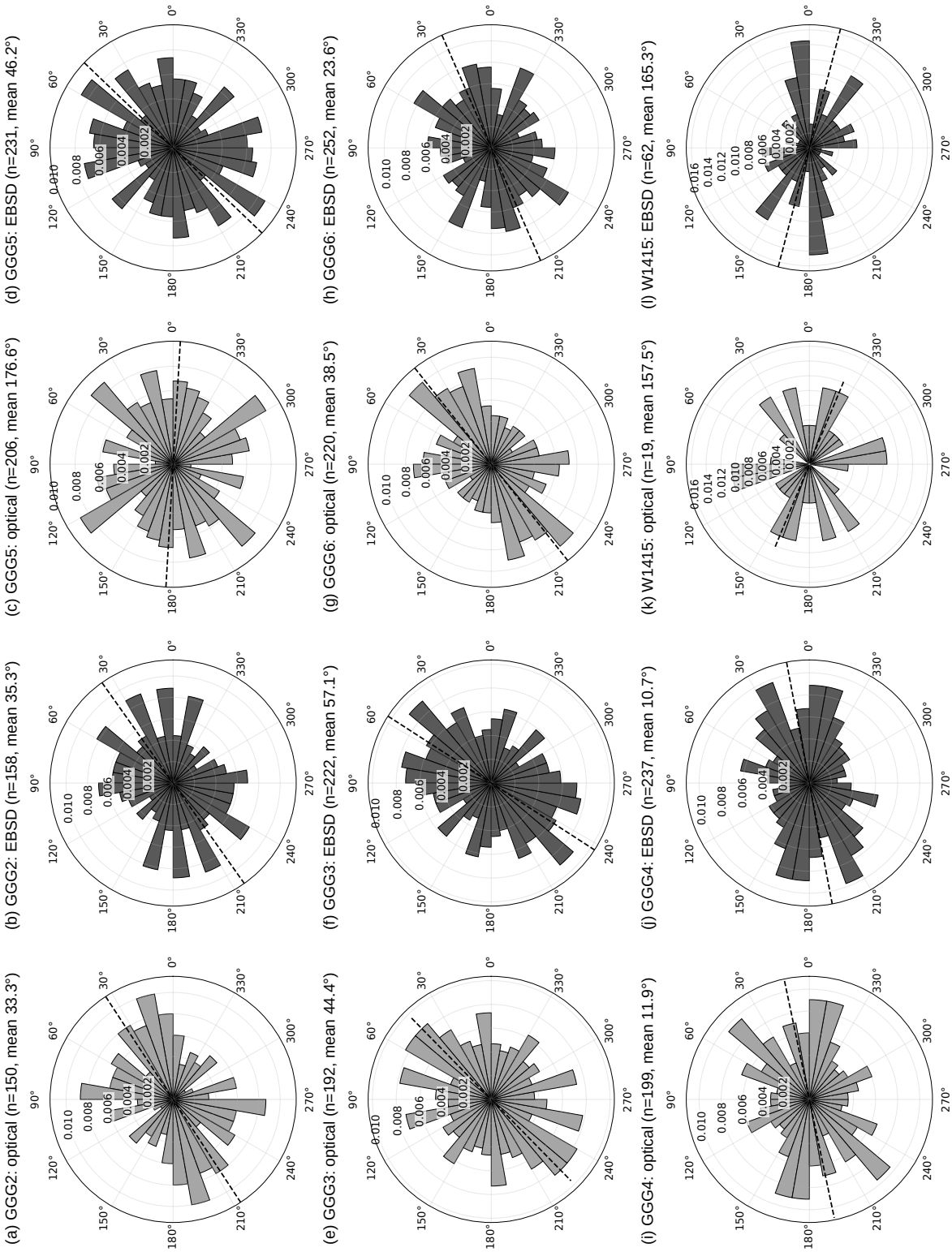


Figure S7: Rose diagrams of grain-shape orientation derived from optical and EBSD grain segmentation for all samples using a 5° segmentation threshold.

References

Huber, P. J. (1964). Robust estimation of a location parameter. *The Annals of Mathematical Statistics*, *35*(1), 73–101. doi: 10.1214/aoms/1177703732

Jones, R. C. (1941). A new calculus for the treatment of optical systems. I. description and discussion of the calculus. *Journal of the Optical Society of America*, *31*(7), 488–493. doi: 10.1364/JOSA.31.000488